Numerical Study of Nozzle Geometry Effects on Three-Dimensional Offset Synthetic Jets

Akili Elizabeth Cyrus

A Thesis

In the Department

of

Mechanical Industrial and Aerospace Engineering

Presented in Partial Fulfillment of the Requirements

for the Degree of Master of Applied Science (Mechanical Engineering) at

Concordia University

Montréal, Québec, Canada

March 2026

CONCORDIA UNIVERSITY

SCHOOL OF GRADUATE STUDIES

This is to certify that the thesis prepared

By: **Akili Elizabeth Cyrus**

Entitled: Numerical Study of Nozzle Geometry Effects on Three-Dimensional Offset Synthetic Jets

and submitted in partial fulfillment of the requirements for the degree of

Master of Applied Science (Mechanical Engineering)

complies with the regulations of the University and meets the accepted standards with respect to originality and quality.

Signed by the final examining committee:

_____ Chair
Dr. Lyes Kadem

_____ Examiner
Dr. Mark Tachie

_____ Examiner
Dr. Lyes Kadem

_____ Supervisor
Dr. Ebenezer Ekow Essel

Approved by _____

Muthukumaran Packirisamy,

Chair, Department of Mechanical, Industrial and Aerospace Engineering

03/31/2026 _____

Mourad Debbabi,

Dean, Gina Cody School of Engineering and Computer Science

Abstract

Numerical Study of Nozzle Geometry Effects on Three-Dimensional Offset Synthetic Jets

Akili Elizabeth Cyrus

This study investigates the influence of nozzle geometry on the unsteady flow characteristics, vortex dynamics, and wall interactions of three-dimensional offset synthetic jets using improved delayed detached eddy simulations (IDDES). Simulations were conducted at a Reynolds number based on the maximum jet-exit velocity and nozzle diameter (d) of $Re_0 = 580$, and at a fixed actuation frequency of 300 Hz. Four nozzle geometries with identical cross-sectional area and an offset height of $2d$ from the wall were examined: circular, square, and rectangular nozzles with aspect ratios of $AR = 3$ and $AR = 1/3$. Instantaneous, phase-averaged, and time-averaged statistics, including the Q-criterion, were used to characterize the evolution of vortex rings, jet-wall attachment, and downstream wall synthetic jet development. The results show that all jets attached to the wall due to the Coandă effect, with the attachment length and mean decay rate decreasing for non-circular nozzles. Circular jets exhibited coherent vortex rings that persisted farther downstream, while square and rectangular jets underwent faster breakdown and enhanced turbulent mixing. Rectangular jets displayed axis switching, generating secondary spanwise vortices and promoting spanwise spreading of near-wall structures. The findings provide new insight into the effect of nozzle geometry in controlling vortex dynamics and wall interactions, with potential applications in the optimal design of offset synthetic jet actuators for enhanced mixing, heat transfer, and flow separation control in fluid-thermal engineering systems.

Acknowledgments

I would like to express my sincere appreciation to my thesis advisor, Dr. Ebenezer Ekow Essel, for his guidance, insight, and unwavering support. The opportunity you gave me has allowed me to grow intellectually in many areas and to appreciate the intricacies of research, as well as the empathy you extended me after a difficult loss. I am also grateful to Dr. Lyes Kadem and Dr. Mark Tachie for agreeing to serve on my thesis committee.

I would also like to thank all past and present members of my home away from home, the Concordia Turbulence Research Lab (CTRL), for their unwavering support and assistance throughout my years in the lab, including my deskmate Dorina (affectionately called Dee), my brother Joseph (Jobro), my summer tea buddy Ana Sofia, and my lunch buddies Luka and Reza.

Finally, I feel incredibly fortunate to have been blessed with the support of such wonderful family and friends throughout my thesis journey, especially after the sudden passing of my father, Dr. James Pemberton Cyrus. I would like to express my thanks to my mother, Gail; my sister, Shanni; Uncle Sheridan, Samara, Abby, Andre, Ben, Mansita and Cara, as well as the rest of my extended family and Gina. I also cannot forget my Montreal friends, Elisa and Kiya. Without your support, this thesis would simply not have been possible.

Dedication

I would like to dedicate this thesis to my late father, Dr. James Pemberton Cyrus, who passed during the beginning of this thesis writing process. From my master's courses, presentations, and coding to the mysterious groundhog on my street, no matter how busy you were, you always made yourself available when I needed a listening ear. Thanks to this, your encouragement and love will forever live on through this thesis.

Table of Contents

List of Figures

List of Tables

Nomenclature

A	Area
a	Amplitude
a_{ij}	Anisotropic tensor
C_{DES}	Fundamental empirical constant of DES
d	Diameter
F_1	Blending function
f	Frequency (HZ)
f_d	Shielding function
$\vec{g}$	Gravitational constant
G/d	Normalized jet offset ratio
h	Height
k	Turbulent kinetic energy
L	Streamwise distance of the flow domain
L_j	Stroke ratio
L_r	Attachment length
l_{DDES}	DDES length scale
l_{RANS}	RANS length scale
N_w	Near wall structures
n	Decay rate of maximum streamwise mean velocity
$\boldsymbol{n}$	Unit normal vector
p	Pressure
PC	Potential core
Q^*	Normalized instantaneous Q-criterion
Q^*_ϕ	Normalized phase averaged Q-criterion
r	Cell radius
r_o	Cavity radius
Re_0	Jet Reynolds number
S	Stokes number
s	Instantaneous diaphragm displacement
$\bar{S}_{ij}$	Mean rate of strain
St	Strouhal number
t	Time
$\boldsymbol{U}$	Mean velocity vector
U	Time averaged velocity
$\boldsymbol{u}$	Velocity vector
U_{cl}	Centreline velocity
U_0	Time-averaged maximum jet exit velocity during the expulsion phase
$U_i(x,y,z)$	Mean of instantaneous velocity component
$u_i(x,y,z,t)$	Instantaneous velocity component
$u_i'(x,y,z,t)$	Fluctuating velocity component
U_m	Maximum streamwise mean velocity
U_p	Peak velocity

$-\overline{uv}$	Time averaged Reynolds shear stress
V	Volume
x_p	Attachment point
y	Wall normal position
$y_{0.5}/d$	Jet width in $x-y$ plane
y_m	Wall normal position of the maximum jet velocity
$z_{0.5}/d$	Jet width in $x-z$ plane
Γ	Circulation
C_μ	Empirical constant
U_ϕ	Phase-averaged jet velocity
U_τ	friction velocity
δ_{ij}	Kronecker delta
$\emptyset$	General property such as velocity, entropy, or enthalpy
λ_{ci}	Swirling strength
λ_2	Hessian of strength criterion
μ	Dynamic viscosity of a fluid
ν	Kinematic viscosity
ν_T	Eddy viscosity
ω	Specific dissipation rate
ω_y	Time averaged wall normal vorticity
$\omega_{\phi y}$	Phase averaged wall normal vorticity
ω_z	Time averaged spanwise vorticity
$\omega_{\phi z}$	Phase averaged spanwise vorticity
ω_z'	Instantaneous spanwise vorticity
ϕ	Phase
Ψ	Low-Reynolds-number correction factor
ρ	Density
τ_{ij}	Reynolds stress tensor
φ_1	Constant or coefficient from the original $k-\omega$ model

Acronyms

AR	Aspect ratios non-circular geometries
ASM	Algebraic Stress Models
AV	Arc like vortices
CCW	Counter-clockwise
CFL	Courant-Friedrichs-Lewy
CVP	Counter-rotating vortex pairs
CW	Clockwise
DDES	Delayed Detached Eddy Simulation
DNS	Direct Numerical Simulation
EASM	Explicit Algebraic Stress Model
FVM	Finite Volume Method
HWA	Hot-wire anemometry
Hybrid-BCD	Hybrid second-order upwind/bounded-central
IDDES	Improved Delayed Detached-Eddy Simulations
LES	Large Eddy Simulation
LRR	Launder-Reece-Rodi
OSJ	Offset Synthetic Jet
PIV	Particle Image Velocimetry
RANS	Reynolds-Averaged Navier–Stokes
RSM	Reynolds Stress Models
SA	Spalart-Allmaras
SGS	smaller subgrid-scale
SJA	Synthetic jet actuator
SSG	Speziale-Sarkar-Gatski
SST	Shear Stress Transport
SV-I	Streamwise Vortices 1
SV-II	Streamwise Vortices 2
TKE	Turbulent Kinetic Energy
WMLES	Wall-Modeled LES
2D	Two-Dimensional
3D	Three- Dimensional

Chapter 1. Introduction

1.1 Motivation

Synthetic jets actuators (SJA) are a type of fluidic device, also known as zero-net-mass flux jets, that form jets entirely from their working fluid. This is very advantageous, and due to this feature, synthetic jets have been used as active flow control devices in many applications such as delaying flow separation in airfoils, cooling of electronics, and jet mixing ([1]–[4]). SJA can generate synthetic jets using periodic motion of a diaphragm or a piston. Here, the focus is on diaphragm-based SJA.

As shown in Figure 1.1, the SJA consists of a cavity with a diaphragm, a neck or nozzle, and an orifice. The bottom of the cavity has an oscillating diaphragm with amplitude (a) and an actuation frequency f. The cavity is connected to a nozzle of diameter d and height h, which is open to the quiescent environment. This type of jet is often referred to as a free synthetic jet.

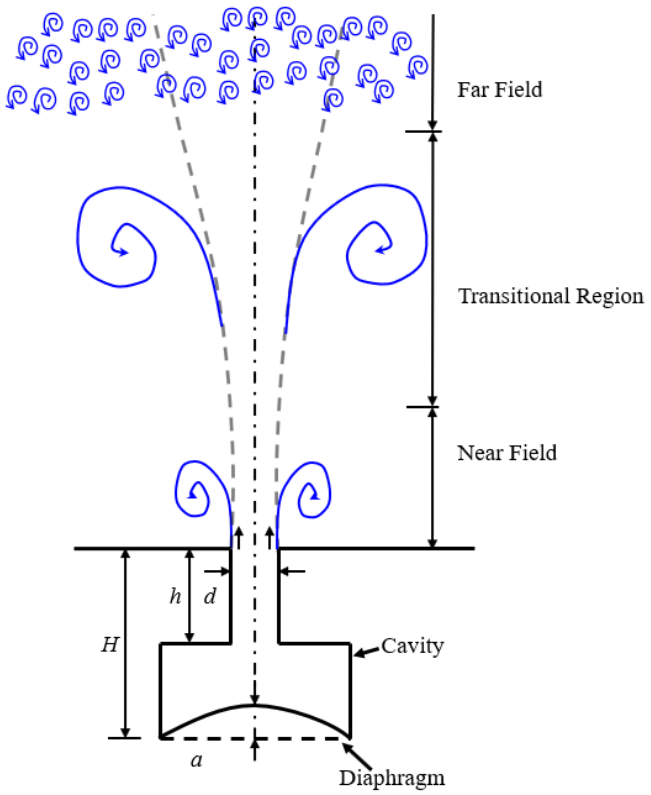

Figure 1.1: A schematic of the salient features and nomenclature of a free synthetic jet.

The operation of the SJA begins with the excitation of the diaphragm, which induces an oscillating pressure within the cavity and causes an alternating suction and ejection of the working fluid. During the ejection phase (also known as the blowing phase), the ejected flow separates at the sharp edges of the orifice and forms a vortex sheet that rolls up into vortex rings, or into a counter-rotating vortex pair (CVP) in two-dimensional (2D) cases. These vortices then convect away from the orifice by their self-induced velocity and transfer linear momentum into the working environment ([5], [6]).

The evolution of the ejected vortices is associated with interesting phenomena such as vortex stretching ([6]–[8]), vortex ring trains [9], vortex build up [10], and axis-switching ([6], [11], [12]).

These phenomena are also influenced by geometric conditions, including the presence of a nearby solid or porous wall, crossflow, and nozzle geometry ([13], [14]).

In applications where the jet is generated directly perpendicular to a wall, it is referred to as an impingement synthetic jet. When the jet is issued parallel to and at an offset distance from a wall, it is referred to as an offset synthetic jet (OSJ) (Figure 1.2). While extensive investigations have been conducted on free synthetic jets and impingement synthetic jets, studies performed on OSJs are rare, and as a result, their flow characteristics are not well understood. Moreover, the effects of nozzle geometry on the vortical structures of OSJs have not been investigated in the open literature. This gap directly impacts the ability to apply existing insights on OSJs toward effective flow control strategies for fluid-thermal engineering applications such as film cooling and the cooling of electronics in data centers.

Literature review

1.1.1 Free synthetic jets

Free synthetic jets have been studied extensively ([2], [8], [13], [15], [16]). The flow field is usually divided into three main regions: the near field, the transitional region, and the far field (Figure 1.1). The near field is located close to the orifice exit and is associated with the formation and convection of discrete vortex rings. In the transitional region, these vortex rings interact and entrain ambient fluid into the jet, which promotes jet spreading. The far field corresponds to the breakdown of the vortex rings into smaller eddies, leading to the formation of a turbulent synthetic jet [5]. In this region, the flow may develop a self-similar state once fully developed ([17], [18]).

The flow characteristics and the evolution of vortex rings in a free synthetic jet are significantly influenced by dimensionless parameters such as the spatially averaged Reynolds number (Re_0),

stroke ratio (L_0), Strouhal number (St), Stokes number (S), nozzle geometry, and aspect ratio, AR = w/l, where w is the width and l is the height of the slot exit for non-circular geometries ([12], [19]). The Reynolds number is defined as:

$$Re_0 = U_0 d/\nu \tag{1.1}$$

where U_0 is the time-averaged maximum jet exit velocity during the expulsion phase, and ν is the kinematic viscosity of the fluid. The time-averaged maximum jet exit velocity is determined as:

$$U_0 = \frac{1}{T}\int_0^{\frac{T}{2}} u_o \, dt \tag{1.2}$$

where u_o is the instantaneous centerline streamwise velocity, $T = 1/f$ is the period of the actuation cycle, $[0, T/2]$ corresponds to the expulsion phase, and t is time. The stroke ratio (L_0) and Strouhal number (St) are defined, respectively, as:

$$L_0 = U_0/(fd) \tag{1.3}$$

$$St = \frac{fd}{U_0} \tag{1.4}$$

The Stokes number is defined as:

$$S = \sqrt{\frac{2\pi f d^2}{\nu}} \tag{1.5}$$

Shuster and Smith [20] investigated the effects of stroke ratio (L_0 = 1, 2 and 3) and Reynolds number (Re_0 = 1000 – 10000) on the flow characteristics of a piston-based free synthetic jet using particle image velocimetry (PIV). The near field was dominated by vortex rings formed during the expulsion phase, and the flow scaled with L_0. In the far field, the synthetic jet resembled a round

turbulent steady jet but decayed faster than a conventional steady jet. For a fixed Reynolds number, the jet momentum was similar at higher stroke ratios, but it increased with increasing Reynolds number.

Zhou et al. [21] conducted a numerical study and found that the formation of a synthetic jet strongly depends on the Stokes number. A minimum Stokes number of $S = 8.5$ was required to ensure appreciable vortex roll-up at stroke ratios $L_0 > 4$.

Chang et al. [15], conducted a numerical study on the effects of Reynolds numbers (Re_0 = 100 – 1588) and Strouhal numbers (St = 0.11, 0.22, 0.33) on the vortex rings of free synthetic jets. The streamwise distance between successive vortex rings decreased with increasing Strouhal number. The combination of low Reynolds number Re_0 = 100, and higher Strouhal numbers (St = 0.22, 0.33) resulted in vortex rings being slowed near the jet exit and eventually merging into a large vortex ring. When Reynolds number was increased to $Re_0 > 676$, vortex rings were shed into the flow field; further increase in Strouhal number enhanced vortex shedding and destabilized the vorticity field.

Li et al [16] performed time-resolved PIV at $Re_0 = 100 - 1588$ and stroke ratios of L_0 = 3.2, 4.8, 6.4 to gain more insight into the flow and formation characteristics of low-Reynolds-number synthetic jets. Between $0 \leq x/d \leq 9$, the number of discrete vortex rings and the primary vortex ring displacement decreased with increasing Strouhal number.

Synthetic jets also greatly depend upon the shape of their nozzle. Shapes such as ellipses, squares, triangles, rectangles, and diamonds have been examined to determine key performance metrics such as efficiency, mixing properties, and flow characteristics ([22]–[25]). One interesting attribute of non-circular nozzles is the phenomenon of axis-switching.

Axis-switching is a well-established phenomenon that occurs in non-circular synthetic jets. In the near-field, as the vortex rings advect downstream, they experience self-induced deformation. This deformation causes a gradual exchange of the major and minor axis (for rectangular nozzles) or a vertex-to-side (for square nozzles) ([26], [27]). Previous experimental and numerical studies ([6], [11], [12], [26], [28]) highlight the importance of aspect ratio in inducing axis-switching.

Chen & Yu [6] investigated the effects of aspect ratios (AR = 1, 1.5, 2, 2.5, 3) on the flow characteristics of rectangular synthetic jets using direct numerical simulation (DNS). The onset of axis-switching behaviour was observed in the near field, and occurred further downstream with increasing aspect ratio. Nozzles with $AR = 1$ showed evidence of 45° axis-switching due to the sharp corners, while nozzles with $AR \geq 1.5$ exhibited 90° axis-switching. The jet cross-sectional profiles evolved from rectangular or square shapes to rounded corners near the nozzle and subsequently deformed into diamond or rhombus-like shapes. Each deformed profile contained a saddle along its major axis, which increased in depth with increasing aspect ratio. After completing axis-switching, the profiles became increasingly axisymmetric downstream.

Van Buren et al. [11] investigated the effects of aspect ratio, $AR = 6, 12$ and 18, on flow structure evolution in quiescent flow at $Re_0 = 615$ and $St = 0.115$ using stereoscopic PIV (SPIV). Jets with lower aspect ratios exhibited higher maximum centerline velocities and faster streamwise velocity decay rates than those with higher aspect ratios. Increasing the aspect ratio strengthened the edge vortices in the major-axis plane, causing them to converge further downstream and widen the spacing between vortex pairs in the minor-axis plane.

Wang et al. [12] conducted a PIV study on synthetic jets with $AR = 1 - 5$, $Re_0 = 166$ and a stroke ratio of 4.5, to investigate the near-field jet evolution. Three successive

axis switches were observed for rectangular jets with of $AR \geq 3$. Axis switching locations were identified by the intersection of jet widths measured in the parallel and vertical planes. They also reported vortex ring shape evolution using 2D and 3D visualizations, with findings consistent with Iio et al. [6] and Chen & Yu [28]. Increasing the aspect ratio accelerated vortex ring deformation.

At $AR = 5$, the primary vortex rings eventually split into two sub-structures downstream. For $AR = 3$, deformation of the primary vortex ring led to the formation of two sub-vortices (I and II), and secondary vortices, SV-I and SV-II, by $x/d = 4$. SV-I were elongated structures located behind the primary vortex ring, and have been observed in previous studies ([21], [29]). SV-II were arc-like structures that detached from the primary vortex, and split into two as the jet evolved downstream. SV-II interacted with shedding vortices that merged with SV-I. This behavior, also reported by Wang et al. [26], enhanced jet entrainment and mixing for $AR = 3$.

Synthetic jets with non-circular nozzles exhibit complex flow phenomena, including vortex ring distortion resulting from axis-switching. However, the effects of an offset wall on these flow phenomena are not well-understood.

1.1.2 Offset synthetic jets

Offset synthetic jets (OSJs) exhibit more complex flow features than free synthetic jets. Based on previous studies of offset steady jets [30] and OSJs ([31], [32]) the salient flow characteristics and nomenclature of OSJs are presented in Figure 1.2. The orifice center is offset by a distance G from the bottom wall of the quiescent environment.

An OSJ consists of three primary regions: the reverse flow region, the attachment region, and the wall synthetic jet region. In the reverse flow region, reduced entrainment beneath the jet generates a low-pressure zone that deflects the jet toward the wall, leading to attachment at the mean

attachment point, x_{rp}. The attachment region corresponds to the streamwise extent over which the instantaneous attachment point fluctuates about x_{rp}. Downstream of x_{rp}, the jet redevelops into a wall synthetic jet with an inner boundary-layer-like region ($y < y_m$) and an outer region ($y > y_m$) that behaves similarly to a free jet ([30], [33]). Unlike offset steady jets, the periodic vortex train produced by SJAs complicates jet–wall interaction; however, due to the limited studies, these mechanisms are not well-understood.

For offset steady jets, previous studies ([30], [34], [35]) have shown that the attachment point increases with increasing offset ratio G/d and is largely independent of Reynolds number. Nyantekyi-Kwakye et al. [35] reported that the decay rate increased with increasing G/d for $0 \leq G/d \leq 8$, while Agelin-Chaab & Tachie [30] found the decay rate to be independent of offset ratio for $G/d \leq 2$ in the far-field self-similar region.

More recently, Hammond et al. [32] investigated the effects of offset height ratio ($G/d = 1 - 4$) on OSJs using improved delayed detached-eddy simulations (IDDES). They found that the attachment point increased with increasing offset ratio. The decay rates of the OSJ were higher than those of the free synthetic jet and increased as G/d decreased. For $G/d = 1$, vortex rings attached almost immediately to the wall, inducing strong spanwise stretching and rapid jet breakdown. In contrast, for $G/d = 3 - 4$, delayed wall attachment allowed vortex evolution similar to free synthetic jets, including far-field self-similarity.

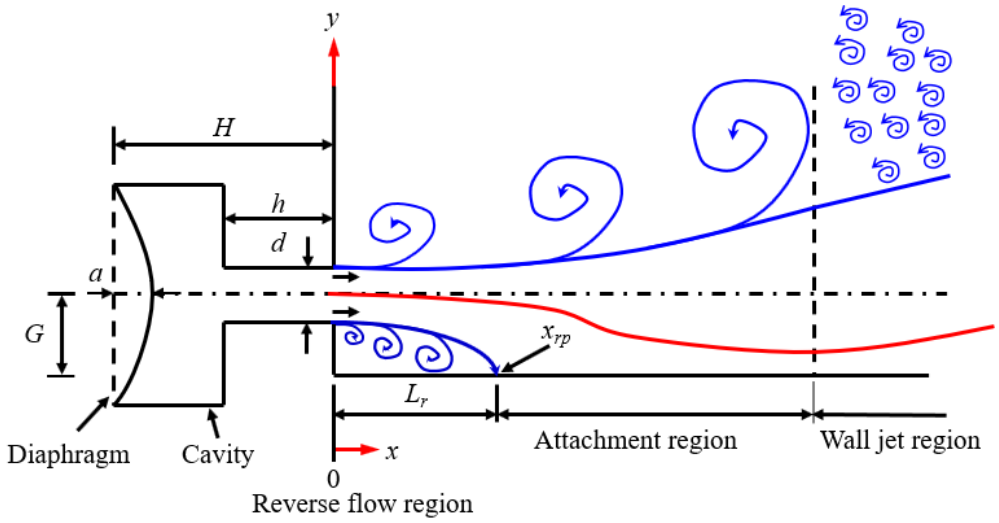

Figure 1.2: A schematic of the salient features and nomenclature of an offset synthetic jet. Not drawn to scale.

Objective

While the effects of nozzle geometry on free synthetic jets have been extensively studied, the influence of nozzle geometry on offset synthetic jets, to the author's knowledge, has not yet been examined in the open literature. In free synthetic jets, non-circular nozzles are known to produce complex flow phenomena such as axis-switching. However, the manner in which the presence of a nearby wall modifies these dynamics in offset synthetic jets remains poorly understood.

Therefore, the objective of this study is to investigate the effects of orifice shape on the interaction of an offset synthetic jet with an adjacent solid wall. To this end, improved delayed detached-eddy simulations (IDDES) were conducted for four nozzle shapes of equal cross-sectional area: a circular orifice, a square orifice with aspect ratio ($AR = 1$), and two rectangular orifices with $AR = 3$ and $AR = 1/3$. All simulations were performed at a fixed actuation frequency and diaphragm amplitude.

Chapter 2. Methodology

In this chapter, the governing equations of fluid flow, consisting of the conservation of mass and conservation of momentum, are introduced. A brief overview of the different turbulence models used in the present study is also presented. A full description of the turbulence models is available in the respective referenced studies, as well as in the STAR-CCM+ User Guide (Siemens Digital Industries Software, 2024).

Introduction

Turbulent flow fields exhibit complex phenomena that can be captured using various numerical approaches, including Direct Numerical Simulation (DNS), Large Eddy Simulation (LES), and Reynolds-Averaged Navier–Stokes (RANS) methods. This thesis uses the Improved Delayed Detached Eddy Simulation (IDDES), a hybrid RANS–LES framework, to resolve the turbulent flow characteristics of the offset synthetic jet issuing from four orifice shapes: a circular orifice, a square orifice with unit aspect ratio, and two rectangular orifices with aspect ratios (AR) of 3 and 1/3.

In the present study, STAR-CCM+, a computational fluid dynamics (CFD) software package, is used to solve the IDDES equations using the finite volume method (FVM). The $k-\omega$ Menter Shear Stress Transport (SST) model was used as the RANS component of the IDDES, where k is the turbulent kinetic energy and ω is the specific dissipation rate. This chapter presents a description of the governing equations and turbulence models used in the study.

Governing equations

To simulate fluid flow accurately, the fundamental conservation laws of mass and momentum must be satisfied. The equation for the conservation of mass is presented Equation (2.1), where t represents time, ρ is density, and $\boldsymbol{u}$ is the velocity vector. The momentum equation states that the rate of change of momentum must equal the sum of forces acting on the fluid, as presented in Equation (2.2), where p is pressure, μ is the dynamic viscosity of a fluid, and $\boldsymbol{g}$ is the gravitational vector. These equations together constitute the Navier-Stokes equations.

$$\frac{\partial \rho}{\partial t} + \nabla \cdot (\rho \boldsymbol{u}) = 0 \tag{2.1}$$

$$\rho \frac{D\boldsymbol{u}}{Dt} = -\nabla p + \rho \boldsymbol{g} + \mu \nabla^2 \boldsymbol{u} \tag{2.2}$$

The Navier-Stokes equations can also be expressed as a transport equation for a general property $\emptyset$, such as velocity, entropy, or enthalpy, as shown in Equation (2.3). The first term on the left-hand side represents the rate of change of $\emptyset$ within the control volume. The second and third terms represent the convective and diffusive transport of $\emptyset$ across the control surfaces, respectively. The final term on the right-hand side represents source terms, such as body forces, which accounts for changes in $\emptyset$ within the control volume due to these sources (Wilcox & David [36]).

$$\int_{\Delta t} \frac{\partial}{\partial t} \left(\int_{CV} \rho \emptyset dV \right) dt + \int_{\Delta t} \int_{A} \boldsymbol{n} \cdot (\rho \emptyset \boldsymbol{u})\, dA dt = \int_{\Delta t} \int_{A} \boldsymbol{n} \cdot (\Gamma_{\emptyset} \nabla_{\emptyset}) dA dt + \int_{\Delta t} \int_{CV} S_{\emptyset} dV dt \tag{2.3}$$

The finite volume method integrates the governing equations over each control volume and then discretizes the transient, convective, diffusive, and source terms associated with $\emptyset$ [37]. In particular, the convective and diffusive terms are evaluated as fluxes across the control volume faces, while the source terms are integrated over the volume. A detailed description of the finite

volume method for solving the Navier-Stokes equations is provided in the STAR-CCM+ User Manual [38] and is not repeated here for brevity.

Turbulence models

There are three main approaches for simulating turbulent flows: DNS, LES, and RANS. All three methods are based on the Navier-Stokes equations, which govern fluid motion. DNS solves the full Navier-Stokes equations without turbulence modeling, resolving all spatial and temporal scales. This makes DNS highly accurate but computationally prohibitive for most engineering applications. LES solves the filtered Navier-Stokes equations, resolving the larger turbulent structures while modeling the smaller, subgrid-scale motions. RANS equations involve time-averaging the Reynolds-decomposed Navier-Stokes equations, modeling all turbulent fluctuations. This approach is computationally efficient but provides a less detailed description of turbulence. Since IDDES, used in the present study, is a hybrid RANS-LES model, brief descriptions of RANS and LES are provided in this section, followed by the governing equations and modeling approach of IDDES ([36], [37], [39]).

2.1.1 Reynolds Averaged Navier-Stokes (RANS)

Reynolds-Averaged Navier-Stokes (RANS) equations are a widely used approach in CFD for simulating turbulent fluid flows. Averaging can be performed using time averaging, spatial averaging, or ensemble averaging. Time averaging is typically applied to statistically steady flows, such as fully developed pipe flow. Spatial averaging is often used for homogeneous turbulent flows. Ensemble averaging is generally employed for unsteady or decaying turbulent flows, where multiple realizations of the same flow are available.

To derive the Reynolds-averaged equations, the instantaneous velocity component, $u_i(\boldsymbol{x}, t)$ is expressed as the sum of its mean component $U_i(\boldsymbol{x})$ and a fluctuating component $u_i'(\boldsymbol{x}, t)$, as shown in Equation (2.4). This procedure is referred to as Reynolds decomposition ([36], [39]).

$$u_i(\boldsymbol{x}, t) = U_i(\boldsymbol{x}) + u_i'(\boldsymbol{x}, t) \tag{2.4}$$

Applying Reynolds decomposition to the Navier-Stokes equations and performing averaging, yields the RANS continuity (Equation (2.5)), and momentum (Equation (2.6)) equations:

$$\nabla \cdot \boldsymbol{U} = 0 \tag{2.5}$$

$$\frac{\partial \boldsymbol{U}}{\partial t} + \boldsymbol{U} \cdot \nabla \boldsymbol{U} = -\frac{1}{\rho}\nabla p + \nu \nabla^2 \boldsymbol{U} + \nabla \cdot \boldsymbol{\tau} \tag{2.6}$$

where $\boldsymbol{U}$ is the mean velocity vector, p is the mean pressure, $\boldsymbol{\tau} = -\overline{u_i' u_j'}$ is the Reynolds stress tensor, representing the momentum transport due to turbulence. The Reynolds stress tensor, $\boldsymbol{\tau}$:

$$\boldsymbol{\tau} = -\overline{u_i' u_j'} = -\begin{bmatrix} \overline{u'^2} & \overline{u'v'} & \overline{u'w'} \\ \overline{u'v'} & \overline{v'^2} & \overline{v'w'} \\ \overline{u'w'} & \overline{v'w'} & w'^2 \end{bmatrix} \tag{2.7}$$

where the diagonal terms represent the Reynolds normal stresses, and the off-diagonal terms represent the Reynolds shear stresses. The RANS momentum equations are inherently complex to solve due to the non-linear convective term, $\boldsymbol{U} \cdot \nabla \boldsymbol{U}$. Moreover, the resulting Reynolds stress tensor, arising from the Reynolds decomposition and averaging procedure, presents the closure problem, where the number of unknowns exceeds the number of equations.

2.1.1.1 Eddy-viscosity and second-moment closure models

To close the RANS equations, turbulence models are employed to predict the Reynolds stresses. The two main approaches used are the eddy-viscosity models and second-moment closure models.

Eddy viscosity models are based on the Boussinesq hypothesis, which assumes that the Reynolds stresses are proportional to the mean rate of strain, $\bar{S}_{ij}$ as follows:

$$-\overline{u_i' u_j'} = \nu_t \left(\frac{\partial U_i}{\partial x_j} + \frac{\partial U_j}{\partial x_i} \right) - \frac{2}{3} k \delta_{ij} = 2\, \nu_T \bar{S}_{ij} \tag{2.8}$$

Here, δ_{ij} is the Kronecker delta, which ensures that $\delta_{ij} = 1$ when $i = j$ and $\delta_{ij} = 0$ when $i \neq j$ ([36], [37], [39]). Examples include the Spalart-Allmaras (SA) model and the two-equation models, such as $k - \varepsilon$, $k - \omega$, and $k - \omega$ SST. These models assume isotropic turbulence and may exhibit limitations in flows with strong curvature, separation or anisotropy. Nonetheless, two-equation models have been successfully applied to simulate a variety of flows, including synthetic jets ([40]–[42]).

Second-moment closure models address some of these limitations by solving additional transport equations for the Reynolds stresses. These models include Algebraic Stress Models (ASM) and Reynolds Stress Models (RSM).

2.1.1.2 $k - \omega$ SST model

This study uses the $k - \omega$ SST model as the RANS component in IDDES. The $k - \omega$ SST, proposed by Menter [43], employs the $k - \omega$ formulation near the wall and gradually transitions to the $k - \varepsilon$ formulation in the outer region using a blending function (F_1):

$$\varphi = F_1 \varphi_1 + (1 - F_1) \varphi_2 \tag{2.9}$$

where φ is a generic turbulence model constant or coefficient used in the $k - \omega$ SST model, φ_1 is the associated variable from the original $k - \omega$ model, and φ_2 is the corresponding variable

derived from the $k-\varepsilon$ formulation. Further details of the model formulation are provided in Menter [43] and are not repeated here for brevity.

2.1.2 Large Eddy Simulation (LES)

Large Eddy Simulation (LES) is a turbulence modeling approach that works by directly resolving the large, energy-containing eddies while modeling the smaller subgrid-scale (SGS) eddies. For high Reynolds number turbulent flows, the smallest eddies tend to be isotropic and exhibit relatively universal behavior, while the large eddies are anisotropic and strongly influenced by factors such as flow geometry, boundary conditions, and other external effects. As a result, for flows that exhibit large-scale unsteadiness, such as unsteady separation, vortex shedding, or coherent structures, LES is generally preferable to RANS models.

LES uses spatial filtering to separate the resolved large-scale motions from the SGS motions. This filtering operation decomposes the instantaneous velocity into a filtered (resolved) component and an SGS component. The filtered velocity field is computed using equations derived from the Navier-Stokes equations, which include an SGS stress tensor that arises from the filtering operation. Similar to the Reynolds stress tensor in RANS, the SGS stresses must be modeled using SGS turbulence models to close the system of equations. The filtered equations are then solved numerically to predict the large-scale flow structures.

LES is less computationally expensive than DNS because it uses a coarser grid and can therefore employ larger timesteps, but it is still significantly more expensive than RANS models. To balance accuracy and computational cost, hybrid RANS-LES approaches have been developed to reduce the computational requirements of LES while preserving its ability to resolve large-scale eddies ([36], [37], [39]).

2.1.3 Improved Delayed Detached Eddy Simulation (IDDES)

The foundation of IDDES is built upon the Delayed Detached Eddy Simulation (DDES) model [44], which itself is an enhancement of the original Detached Eddy Simulation (DES) [45]. These hybrid RANS-LES models were developed primarily for simulating separated flows, where the RANS component is applied to the near-wall attached boundary layer and the LES component is used in the separated flow region. This approach provides a balance between computational cost and accuracy when compared to full LES.

However, a major challenge with DES and DDES is the mismatch that can arise between the RANS and LES regions, particularly within the logarithmic layer. The RANS component forms an “inner” logarithmic layer determined by wall-distance modeling, while the LES component generates an “outer” logarithmic layer governed by the local grid spacing. When the grid spacing becomes sufficiently small relative to the wall distance, the model may prematurely switch to LES inside the boundary layer. This results in a log-layer mismatch, an inaccurate mean velocity profile, and an underprediction of skin friction.

IDDES, proposed by Shur et al. [46], addresses this issue by introducing a shielding function that delays the transition from RANS to LES near the wall, thereby reducing log-layer mismatch and improving the accuracy of wall-bounded turbulent flow simulations. The IDDES model employs a unified formulation that blends DDES with Wall-Modeled LES (WMLES), allowing complex flows to be simulated within a single framework. In addition, IDDES incorporates a modified SGS length scale that depends on both the wall-normal distance and the local grid spacing, rather than on grid spacing alone. Finally, IDDES operates in two modes (DDES and WMLES) depending on the level of resolved turbulence in the inflow. For cases without turbulent inflow, such as synthetic jets, the model follows the DDES branch [44].

Within IDDES, the DDES branch modifies the RANS length scale (l_{RANS}) by replacing it with the DDES length scale (l_{DDES}), defined in Equation (2.10):

$$l_{DDES} = l_{RANS} - f_d \max\{0, (l_{RANS} - l_{LES})\} \tag{2.10}$$

The shielding function, f_d is given as:

$$f_d = 1 - \tanh[(8r_d)^3]] \tag{2.11}$$

The variable r_d, adopted from the Spalart–Allmaras (SA) turbulence model, serves as a wall-distance-based marker, with values close to 1 in the logarithmic layer and close to 0 in free shear flows. The LES length scale l_{LES} appearing in Equation (2.10) is defined as:

$$l_{LES} = C_{DES} \Psi \Delta \tag{2.12}$$

where Ψ is a low-Reynolds-number correction factor and C_{DES} is the fundamental empirical constant of DES [45]. For turbulence models such as $k - \omega$ SST, which do not include an explicit low-Reynolds-number correction, $\Psi = 1$. The original RANS length scale for $k - \omega$ SST model is defined as:

$$l_{RANS} = \frac{\sqrt{k}}{(C_\mu \omega)} \tag{2.13}$$

where $C_\mu \approx 0.09$ is an empirical constant. A complete formulation of IDDES, including the transport equations and constitutive relations, is provided in Shur et al. [46] and is not repeated here for brevity.

In the present study, the governing equations were solved using the finite volume method with an implicit second-order temporal discretization and a hybrid second-order upwind/bounded-central (Hybrid-BCD) convection scheme.

Chapter 3. Numerical setup and validation

This chapter presents the numerical setup and validation of this thesis, aimed at investigating the effect of nozzle geometry on the flow characteristics and vortical structures of offset synthetic jets issuing into a quiescent flow domain.

Model setup

The synthetic jet actuator (SJA) used in the present study has a cavity with a diameter of 30.8 mm and a height of 10 mm, and a neck with a diameter of d = 2 mm and a height of h =10 mm. The SJA model was designed to match the actuator used in the experiments performed by Feero et al. [47] to facilitate validation using the experimental results. To model the quiescent external flow, a cuboid domain, shown in Figure 3.1(a), with a width, depth, and height of 50d was created and attached to the jet exit of the SJA domain. The quiescent flow domain was sized to prevent any backflow at the outlet. Based on the studies by Hammond et al. [32], the SJA was positioned at the midspan of the quiescent flow domain and at a fixed offset height ratio of $G/d = 2$ from the bottom wall. This offset height ratio ensured that the synthetic jet developed sufficiently before interacting with the bottom wall.

To investigate the effect of the aspect ratio (AR) on the offset synthetic jet, three additional SJA models (a square nozzle and two rectangular nozzles) were created with the same cross-sectional area ($\pi\ mm^2$) as the circular nozzle. The dimensions of the circular, square, and rectangular nozzles with $AR = 3$ and $AR = 1/3$ are shown in Figure 3.1(b). Following Wang et al. [12] on free synthetic jets, these aspect ratios were selected to induce axis-switching phenomenon.

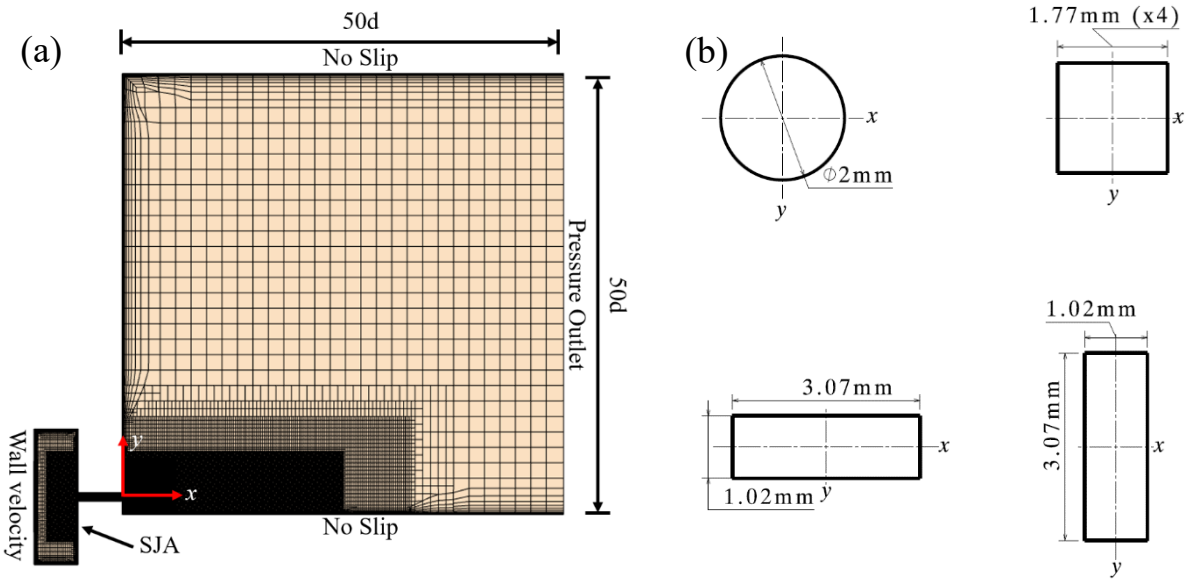

Figure 3.1: (a) Computational domain showing the mesh configuration, boundary conditions and (b) cross-sectional views of the nozzles of the offset synthetic jets investigated.

Mesh

In this study, a multi-block structured mesh was used to model both the quiescent flow and the SJA as shown in Figure 3.2. Four refinement zones were applied to the quiescent flow and SJA domains, with the highest mesh density assigned to the neck and exit of the synthetic jet. The mesh achieved an average of $y^+ < 1$, where $y^+ = yU_\tau/\nu$, U_τ is the friction velocity and $\nu = 1.57 \times 10^{-5}\, m^2/s$ is the kinematic viscosity of air at 25 ˚C, as well as, an average Courant-Friedrichs-Lewy (CFL) number of $\overline{CFL} < 1$. The mesh was created in STAR-CCM+ using the prism layer mesher, surface remesher, and trimmer options. The trimmer option in STAR-CCM+ can generate either hexahedral or polyhedral (dodecahedral) cells; in this study, hexahedral cells were chosen. The trimmer cell mesher produces a robust, high-quality grid for complex geometries by generating a hexahedral core mesh that is trimmed at the boundaries of the input surface [38].

Different refinement zones in the mesh use varying prism layer selections to ensure a smooth transition to the core mesh.

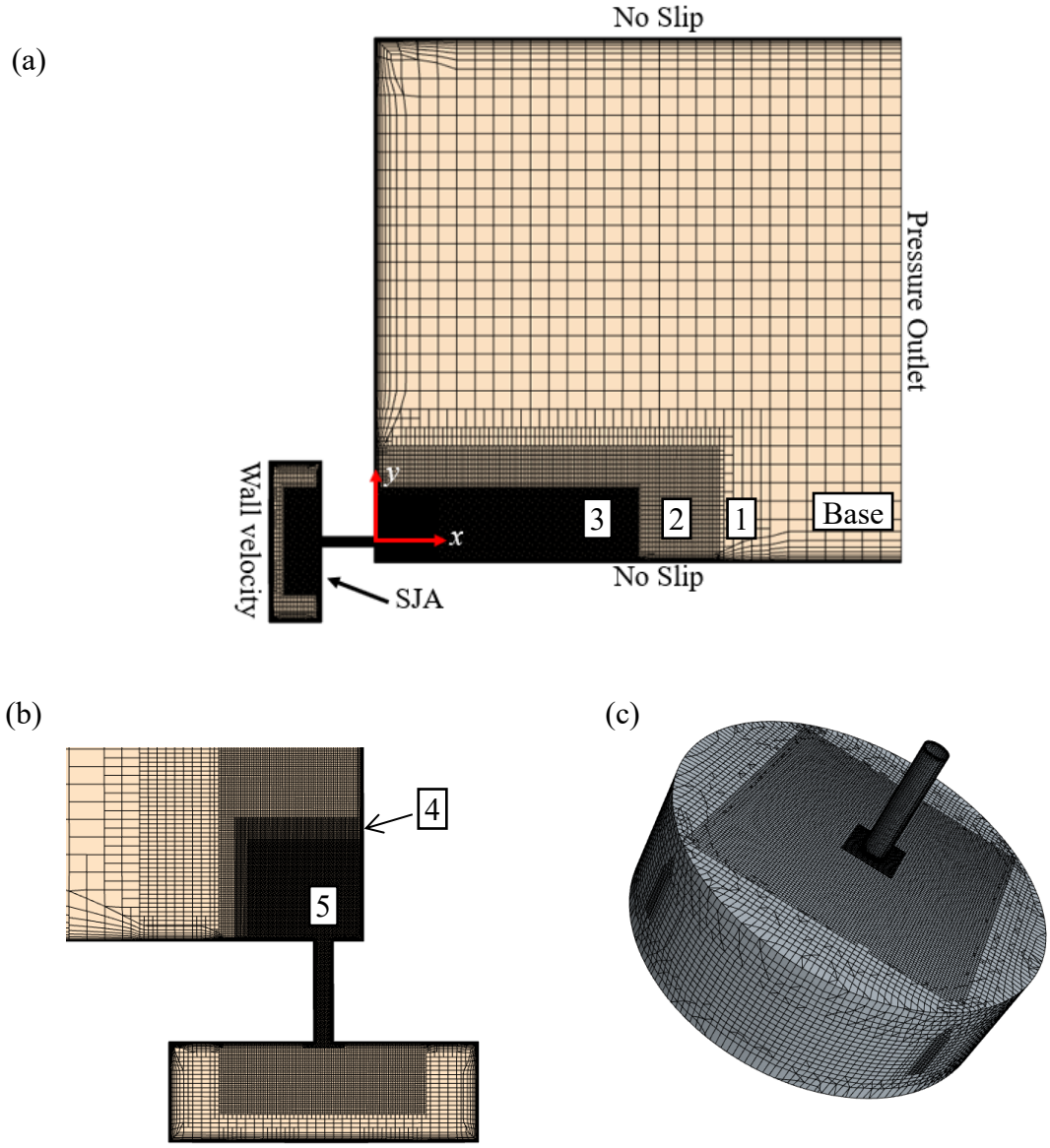

Figure 3.2: (a) Computational domain with labelled refinement regions, (b) zoomed view of the jet exit and SJA and (c) isometric view of the SJA mesh

Boundary conditions

To simulate fluid flow, appropriate boundary conditions must be applied to the computational domain. These boundary conditions allow the solver to compute the solution of the governing equations. The boundary conditions used in this study, shown in Figure 3.2, were applied to both the SJA and the quiescent flow domain.

The quiescent flow domain was modeled as a six-sided cuboid, with a boundary condition applied to each surface. The outlet (right surface) of the domain was designated as a pressure outlet with a gauge pressure of 0 Pa. The remaining five surfaces were assigned no-slip wall conditions, which ensured that the offset synthetic jet was issued adjacent to a wall.

The SJA domain consists of four surfaces: the actuator, cavity walls, cavity top, and nozzle. All surfaces of the SJA domain were assigned no-slip wall conditions. The actuator surface was additionally assigned a morphing motion to simulate the oscillation of the diaphragm. The diaphragm oscillation is modeled using a user-defined function (UDF), shown in Equation. (3.1), which has a parabolic shape with a maximum deflection of amplitude a at the center of the diaphragm, reducing to zero at the cavity walls. The UDF outputs the morpher total linear displacement, defined as the instantaneous diaphragm displacement s for a given cell radius r, with the cavity radius denoted as r_o.

$$s = a\left(1 - \left(\frac{r}{r_o}\right)^2\right) sin(2\pi f t) \tag{3.1}$$

For each test case, the SJA was driven at f = 300 Hz with amplitude, a = 32 μm. The resulting Reynolds number was Re_0 = 580.

Data collection

Data were sampled for flow analysis, including both qualitative and quantitative results. Each simulation was run for a total of 0.176 seconds, corresponding to 12 flow-through cycles, L/U_0, where L is the streamwise distance of the flow domain and U_0 is the spatially averaged jet velocity. To avoid collecting data during the startup period, the simulations were first run for two flow-through cycles (0.0293s), after which data was collected over 43 actuation cycles (0.146s). The residuals for each case stabilized at values below 10^{-5}. For each simulation, instantaneous, time-averaged, and phase-averaged statistics were collected at phase angles of 0°, 45°, 90°, 135°, 180°, 225°, 270°, and 315°.

Mesh sensitivity test and validation

3.1.1 Mesh sensitivity test

A grid convergence test in CFD is used to reduce discretization error arising from the numerical solution of the governing flow equations. To ensure that such errors remain acceptably low, the mesh must be refined until further grid refinement produces no significant change in the solution, while avoiding excessive computational cost [48]. In the present study, three meshes with approximately 3.1, 4.4 and 6.2 million cells were evaluated. The mean centreline velocity, U_{cl} was selected as the primary metric for comparing mesh performance, as shown in Table 3.1, along with the corresponding y^+ values, and CFL numbers for each mesh. In the table, the percentage error between the predicted U_{cl} and the corresponding result of the experimental work by Feero et al. [47] is also presented. All meshes achieved $y^+ < 1$, and a $\overline{CFL} \leq 1$. Within the regions of interest (the quiescent flow domain and the SJA), the maximum CFL remained below 1. At the edge of

the nozzle exit, a small number of cells exhibited local CFL values in the range of 1–3, which is still within the acceptable limits for stability and accuracy when using an implicit solver.

Table 3.1: Mesh sensitivity test parameters

Mesh	Total cell count $\times 10^6$	y^+	U_{cl}	CFL	$\overline{CFL} \times 10^{-4}$	U_{cl} Error (%)
Coarse	3.1	0.73	7.55	1.93	1.00	0.66
Medium	4.4	0.73	7.51	2.77	1.22	0.13
Fine	6.2	0.75	7.51	1.95	1.34	0.13
Feero et al. (experiment)	-	-	7.50	-		-

Additionally, to ensure that the mesh was converging toward a grid-independent solution, the maximum streamwise mean velocity distributions of the circular offset SJA obtained from the three meshes are shown in Figure 3.3. The results indicate that the fine and medium meshes exhibit similar trends, with the medium mesh showing an average maximum deviation of 5.6% relative to the fine mesh, compared to 20.4% for the coarse mesh. Based on this assessment and the results presented in Table 3.1, the medium mesh was selected for the remaining simulations to reduce computational cost while maintaining adequate accuracy.

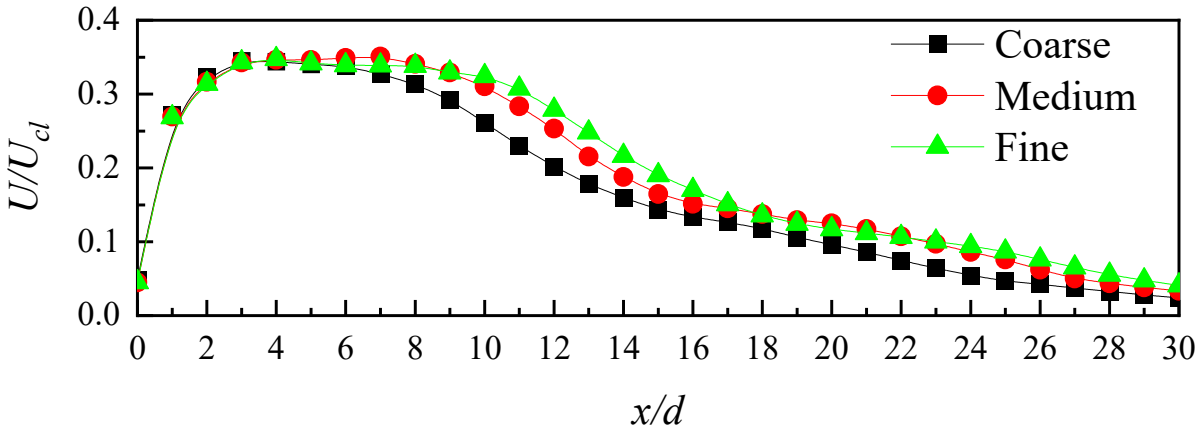

Figure 3.3: (a) Streamwise evolution of the maximum streamwise mean velocity for three mesh sizes (coarse medium and fine mesh) for the circular offset SJA.

3.1.2 Validation

The present study was validated using the cylindrical cavity test case from the free synthetic jet experiments of Feero et al. [47]. In their work, hot-wire anemometry (HWA) was used to measure the radial exit velocity profiles of a free synthetic jet for various cavity geometries and actuation frequencies. Figure 3.4 presents the phase-averaged streamwise velocity (U_ϕ) profiles at the maximum expulsion phase ($\phi = 90$) and the maximum ingestion phase ($\phi = 270$).

The U_ϕ profiles were extracted at the same location as in Feero et al. [47], i.e., near the jet exit at $x/d = 0.075$, and normalized by the mean centreline velocity (U_{cl}) and the nozzle diameter d. The expulsion phase of the synthetic jet is characterized by a top-hat-shaped profile, typical of developing jet flows. The peaks of this top-hat distribution occur at $y/d = \pm 0.4$, in both the experiments of Feero et al. [47] and the present study.

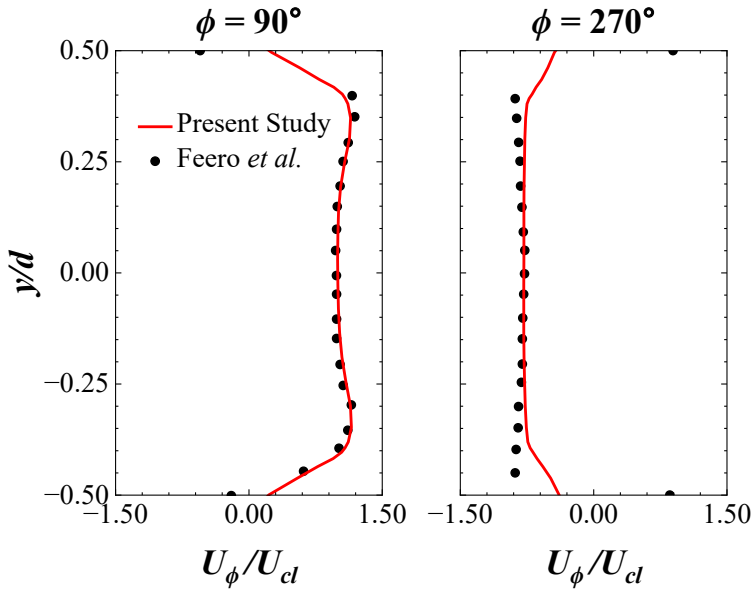

Figure 3.4: Profiles of the phase-averaged streamwise velocity U_ϕ at jet exit, $x/d = 0.075$; normalized by the maximum centerline velocity U_{cl}

The ingestion phase involves the suction of fluid into the cavity, producing a sink-like flow with negative streamwise velocity. The present results reproduce this behavior; however, the velocities near $y/d = \pm 0.5$ are underpredicted compared with the experiment. Feero et al. [47] reported significant uncertainty in the measured velocities at $y/d = \pm 0.5$, as the hot wire cannot distinguish flow direction and may be influenced by strong radial velocity components near the orifice. The radial component is dominant at the orifice edge and may therefore be overrepresented in the experimental data. Overall, the present phase-averaged profiles show good agreement with the experimental measurements within numerical and experimental uncertainties.

Chapter 4. Results and discussion

This chapter presents the results and discussions on the effects of nozzle geometry on the instantaneous, time-averaged, and phase-averaged flow characteristics of the offset synthetic jets.

Instantaneous vortical structures

The instantaneous vortical structures are used to examine the effects of nozzle geometry on the unsteady evolution of the offset synthetic jet interacting with the wall. Several techniques including the Q-criterion [49], swirling strength (λ_{ci}) [50], and the Hessian of the pressure (λ_2 criterion) [51] have been used in the literature to educe the vortical structures without any bias of the mean shear. In the present study, the Q-criterion is used, which is defined as the second invariant of the velocity gradient tensor:

$$Q > \frac{1}{2}(\|\Omega\|^2 - \|S\|^2) \tag{4.1}$$

where Ω denotes the rotational tensor, i.e., the antisymmetric part of the velocity-gradient tensor, and S denotes the rate-of-strain tensor, corresponding to the symmetric part of the velocity-gradient tensor. A positive Q-criterion ($Q > 0$) represents regions where the local rotational rate dominates over the strain rate, identifying the vortical structures within the flow field [52].

Figure 4.1 shows iso-surfaces of the representative normalized instantaneous Q-criterion, $Q^* = Qd^2/U_0^2 = 0.17$ for the offset synthetic jet issuing from the circular, square and rectangular ($AR = 3$ and $1/3$) nozzles, where d is the reference circular nozzle diameter and U_0 is the maximum jet exit velocity for each nozzle. The iso-surfaces are coloured by the normalized instantaneous spanwise vorticity, $\omega_z' d/U_0$, to reveal the rotational direction of the vortices, where

negative and positive vorticity represent clockwise (CW) and counter-clockwise (CCW) rotating structures, respectively. For the circular case, a circular vortex ring forms at the nozzle exit. As the ring advects downstream, it becomes increasingly deformed, generating tail-like structures in its wake. Further downstream, the vortex ring deflects towards the wall due to Coandă effect and eventually attaches to the wall, leading to enhanced breakdown into hair-pin-like structures and spanwise stretching of these vortices. For the square case, a square-shaped vortex ring is generated at the nozzle exit and subsequently attaches to and interacts with the wall. For the rectangular cases, the vortex ring formed at the exit is initially aligned with the nozzle orientation; however, these rings undergo axis-switching prior to impinging on the wall.

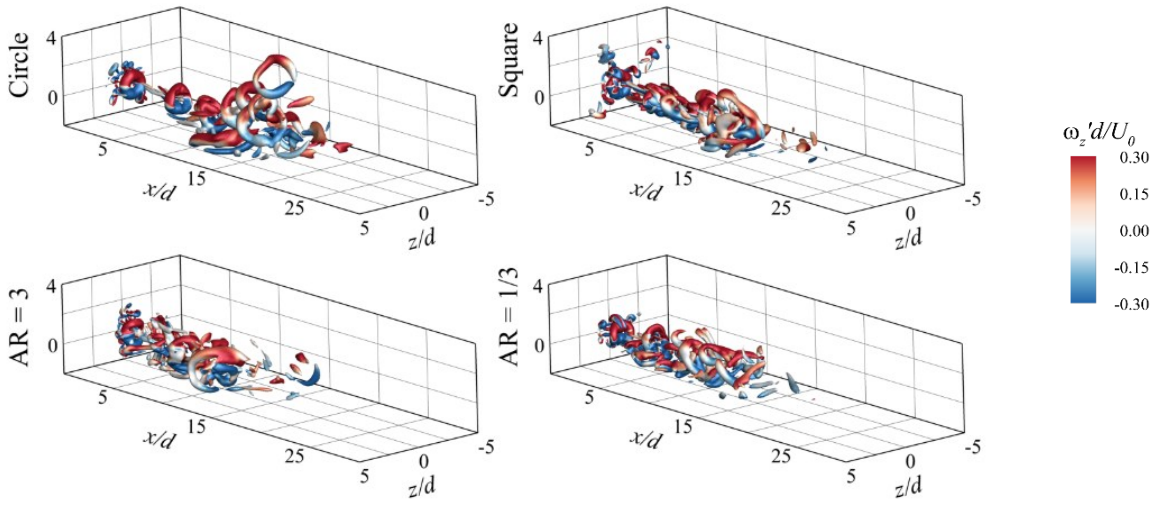

Figure 4.1: Iso-surfaces of instantaneous Q-criterion ($Q^* = Qd^2/U_0^2 = 0.02$) for each test case colored by the normalized instantaneous spanwise vorticity, $\omega_z' d/U_0$.

Phase-averaged statistics

In this section, phase-averaged statistics are used to highlight the coherent, periodic flow structures within the offset synthetic jets. Phase averaging was performed for eight phases within the actuation cycle; however, only the relevant phases are presented for brevity to discuss the effects of nozzle geometry.

Phase-averaged vortical structures

To visualize the evolution of the vortical structures and their interaction with the wall, phase-averaged iso-surfaces of the Q-criterion, $Q^* = Qd^2/U_0^2 = 0.02$, for each test case are presented in Figure 4.2. The plots present the expulsion phases ($\phi = 90°$ and $135°$) and the ingestion phases ($\phi = 225°$ and $270°$), for brevity. The $Q^*$is coloured by the normalized phase-averaged spanwise vorticity at each phase. It is worth noting that, although the phases are correlated with the actuation cycle, they represent different stages of jet evolution downstream of the nozzle exit. Accordingly, the various stages of the vortex-ring evolution identified in the plots are labeled A–D.

For the circular case, each phase exhibits three distinct vortex rings (A-C) that bend toward the wall, with the C-labeled ring interacting directly with the wall. The preceding rings undergo substantial deformation and break down into smaller structures due to wall interaction, evident downstream of the C-labeled vortex. Trailing vortices, formed due to vortex pinch-off - a process in which the leading vortex ring separates from the trailing shear layer during vortex formation near the jet exit [12] are also observed between the distinct vortices (A-C).

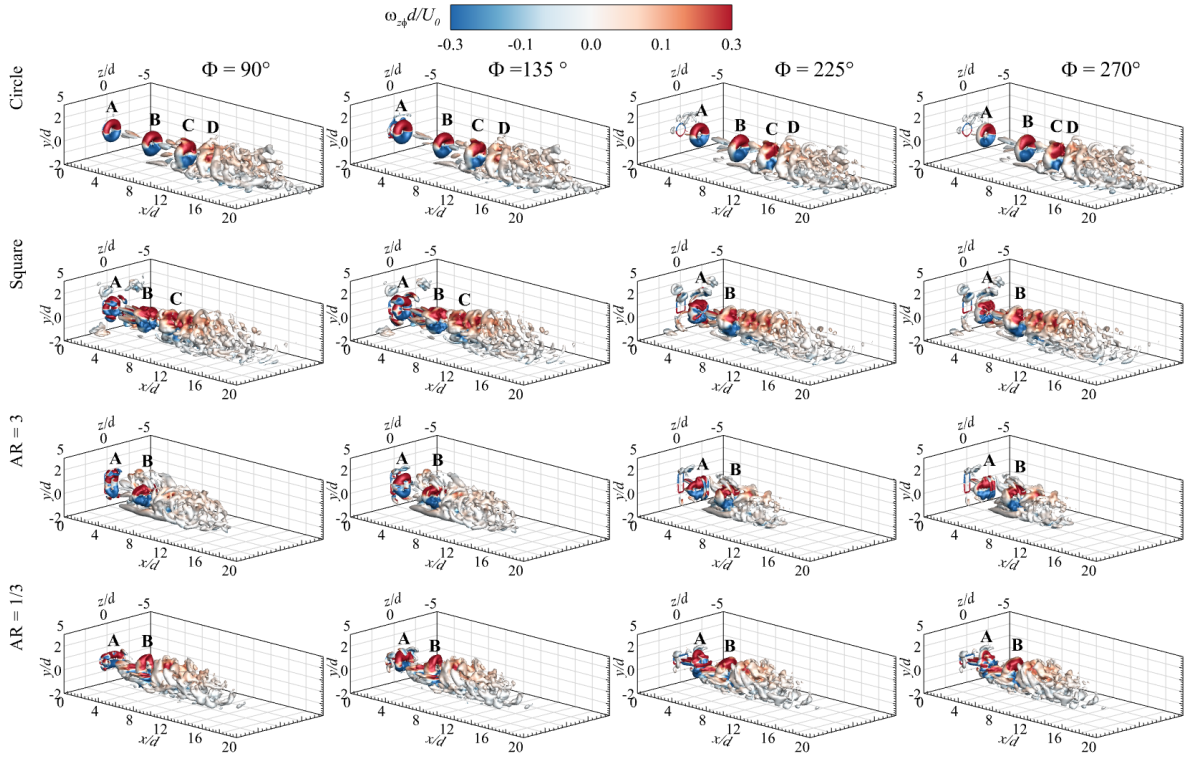

Figure 4.2: Iso-surfaces of phase-averaged Q-criterion $Q^* = Qd^2/U_0^2 = 0.02$ colored by normalized phase-averaged spanwise vorticity for each test case.

Unlike the circular jet, only two distinct vortex rings (A and B) are observed for the square nozzle, indicating earlier deformation. The vortex ring A near the exit exhibits a square shape consistent with the nozzle geometry at $\phi = 90°$, with figure-like structures protruding near each corner. These structures are generated by the vena contracta effect and promote early deformation, rounding the ring edges, as evident in the B-labeled vortex. Trailing vortices between A and B are more pronounced than in the circular case; however, vortex breakdown and decay from wall interactions occur more rapidly in the square jet than in the circular jet.

For the rectangular nozzles, the vortex transition and interaction with the wall are more complex; therefore, additional top and side views of the iso-surfaces at $\phi = 225°$ are shown in Figure 4.3

to provide a more complete description of the vortex features. Figures 4.2 and 4.3 shows that the number of distinct vortex rings is reduced to one (A), which reflects the shape and orientation of the rectangular nozzles. Similar to the square case, the A vortex exhibits figure-like projections near the corners at $\phi = 90°$ and $135°$, causing the rectangular vortex ring to deform at the corners and transition to an elliptical shape. At phases $\phi = 225°$ and $270°$, the A vortex demonstrates $90°$ axis switching for both test cases. Based on the Biot-Savart law ([27], [53], [54]), the axis switching is due to self-induced deformation associated with the azimuthal non-uniform curvature of the elliptically formed vortex ring, leading to an interchange of the major and minor axes relative to their initial orientation ([6], [12], [22], [26], [27]). The reoriented A vortex is also associated with additional structures, including streamwise vortices (SV-I) and arc-like vortices (AV) (Figure 4.3), consistent with similar structures previously reported for rectangular synthetic jets (Wang et al. [12]). The SV-I forms along the inner side near the trailing end of the vortex ring, while the AV wrap around the upstream edges of the vortex along the minor axis. The SV-I structures emerge from deformation of the vortex ring corners, while the AV form ahead of the primary vortex ring as part of the deformation associated with axis switching. For $AR = 1/3$, the reoriented vortex (labeled B) has its major axis perpendicular to the wall, leading to stronger wall interactions compared to the other test cases, as well as backward tilting of the structures during wall interaction. On the other hand, axis switching in $AR = 3$ promotes the development of more pronounced near-wall structures. (N_w).

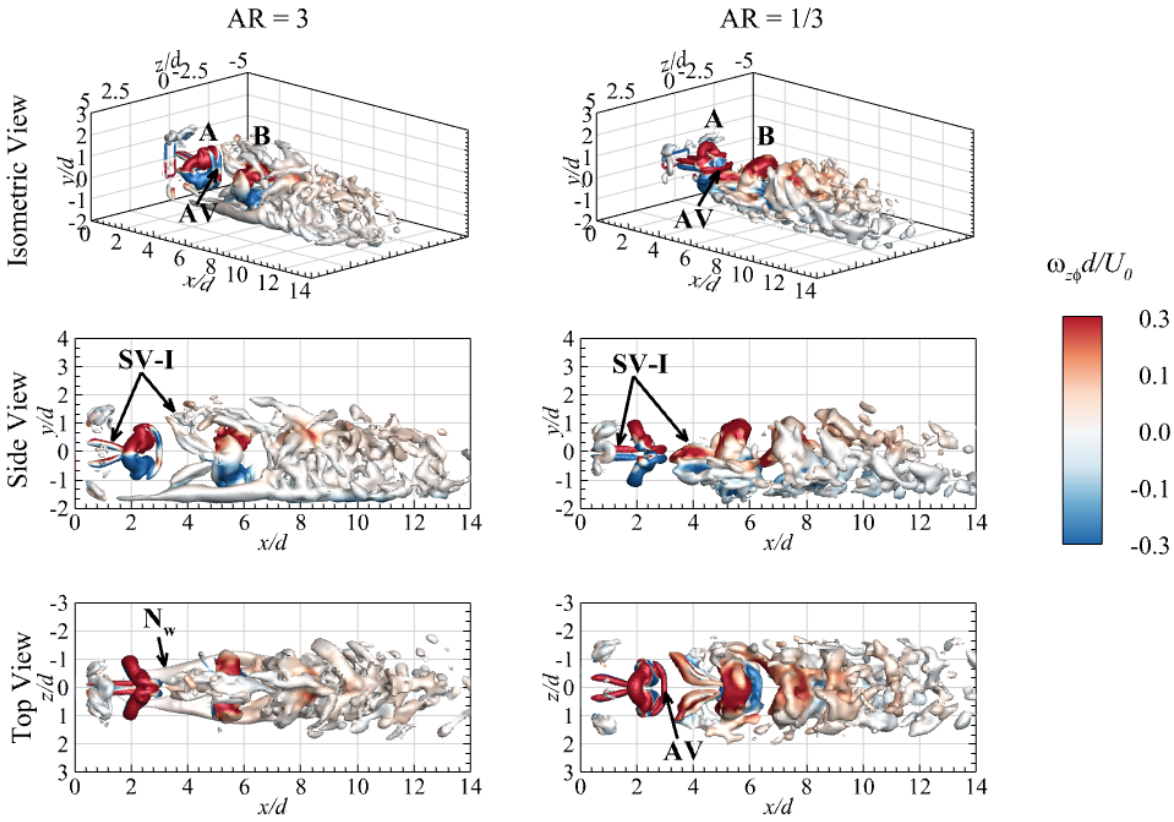

Figure 4.3: Iso-surfaces of phase-averaged Q-criterion ($Q^* = Qd^2/U_0^2 = 0.02$) colored by normalized phase-averaged spanwise vorticity ($\omega_{z\phi}d/U_0$) at $\phi = 225°$ for the rectangular jets.

Phase-averaged flow fields

The effects of nozzle shape on the spatio-temporal evolution of the offset synthetic jet are examined using the out-of-plane phase-averaged vorticity component in the $x-y$ ($z/d = 0$) and $x-z$ ($y/d = 0$) planes during the expulsion ($\phi = 90^\circ$ and 135°) and ingestion ($\phi = 225^\circ$ and 270°) phases, as shown in Figure 4.4. It is worth noting that, due to jet curvature, the $x-z$ ($y/d = 0$) plane does not coincide with the jet centerline, particularly downstream of attachment; consequently, only portions of the vortex cores are captured in this plane as the jet evolves downstream.

For each test case, a primary vortex ring grows at the nozzle exit during expulsion phases, with a trailing shear layer behind it. During the ingestion phases, the vortex ring is shown pinching off and detaching from the trailing jet. Each ring contains CW and CCW vorticity cores, which form a counter-rotating vortex pair (CVP). As each CVP evolves downstream, the CW core interacts with the wall, contributing to the generation of vorticity at the wall as the wall synthetic jet develops.

The circular case (Figure 4.4(a)) has the most distinct pairs visible at phase $\phi = 90^{\circ}$, which reduce from four to three during the suction phase at $\phi = 270^{\circ}$. The square case (Figure 4.4(b)) has two distinct pairs at $\phi = 90^{\circ}$ in the $x - y$ plane, and at the beginning of the suction phase $\phi = 225^{\circ}$. The CVP experiences vortex tilting after attaching to the offset wall ($x/d > 5$), which causes the CCW half to connect to preceding CCW core, leading to the formation of an elongated vortex structure at $\phi = 270^{\circ}$. In the horizontal plane, the vortices remain as three discrete CVP due to the position of the plane.

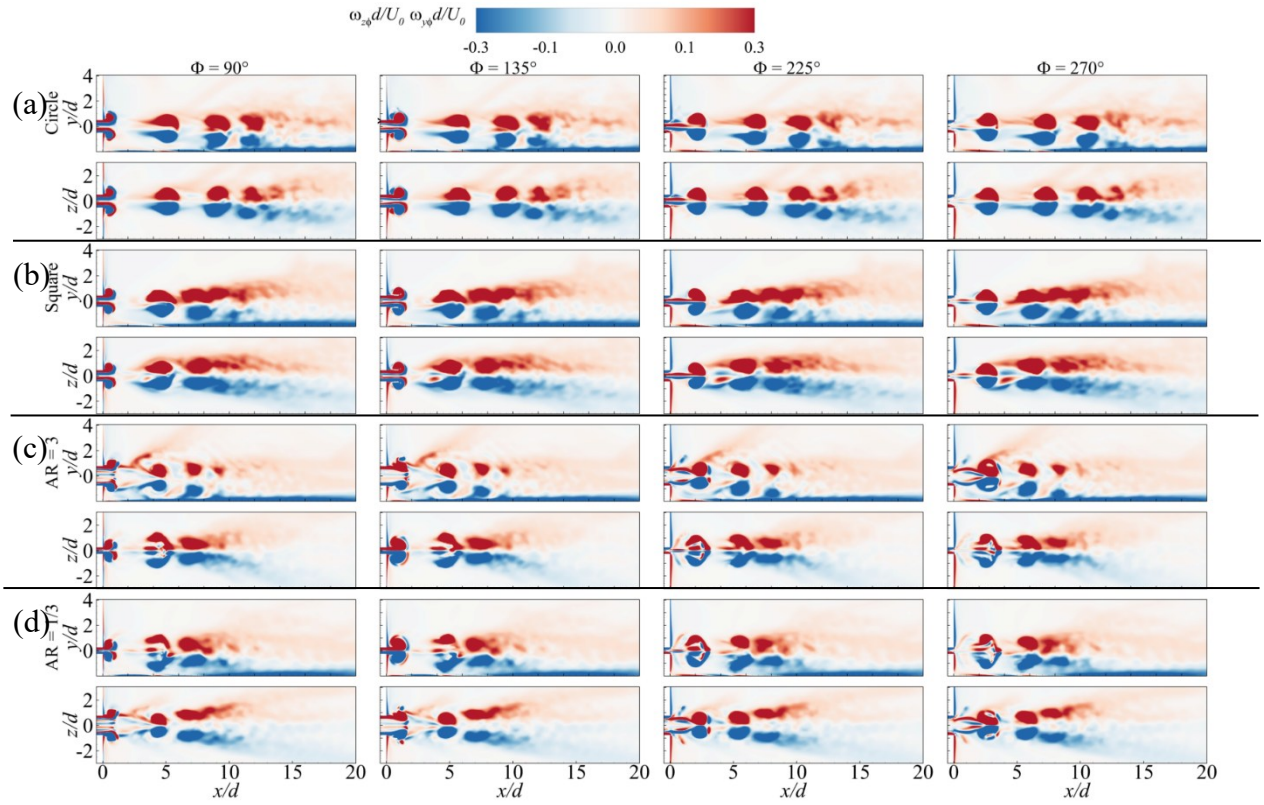

Figure 4.4: Contours of normalized phase-averaged spanwise vorticity ($\omega_{z\phi}d/U_0$) and wall normal vorticity ($\omega_{y\phi}d/U_0$): Circle, Square, $AR = 3$ and $AR = 1/3$, in the $x-y$ symmetry plane and the $x-z$ plane at $y/d = 0$.

For $AR = 3$ (Figure 4.4(c)) and $AR = 1/3$ (Figure 4.4(d)), the vertical and horizontal planes show multiple bands of CW and CCW vorticity near the nozzle exit and between the first two CVPs. These bands correspond to the SV-I structures shown in Figure 4.3. The CW half of the CVP for $AR = 1/3$ deforms and disintegrates earlier than the corresponding structures for $AR = 3$ due to the orientation of the axis-switched vortex, which promotes stronger wall interactions.

Figure 4.5 presents the contours of normalized phase-averaged streamwise velocity for each test case. At peak expulsion phase, $\phi = 90^{\circ}$, a bulb of velocity is expelled from the jet exit; however,

the velocity decreases downstream as the momentum is transferred to the surrounding fluid through entrainment, leading to the eventual decay of the jet. In the vertical symmetry plane, each jet bends towards the offset wall due to the Coanda effect induced by the offset wall. The rectangular jets deform and decay faster than the other test cases due to the effects of axis switching, while self-induced deformation at the edges of the square jet promotes earlier deformation and decay compared with the circular jet.

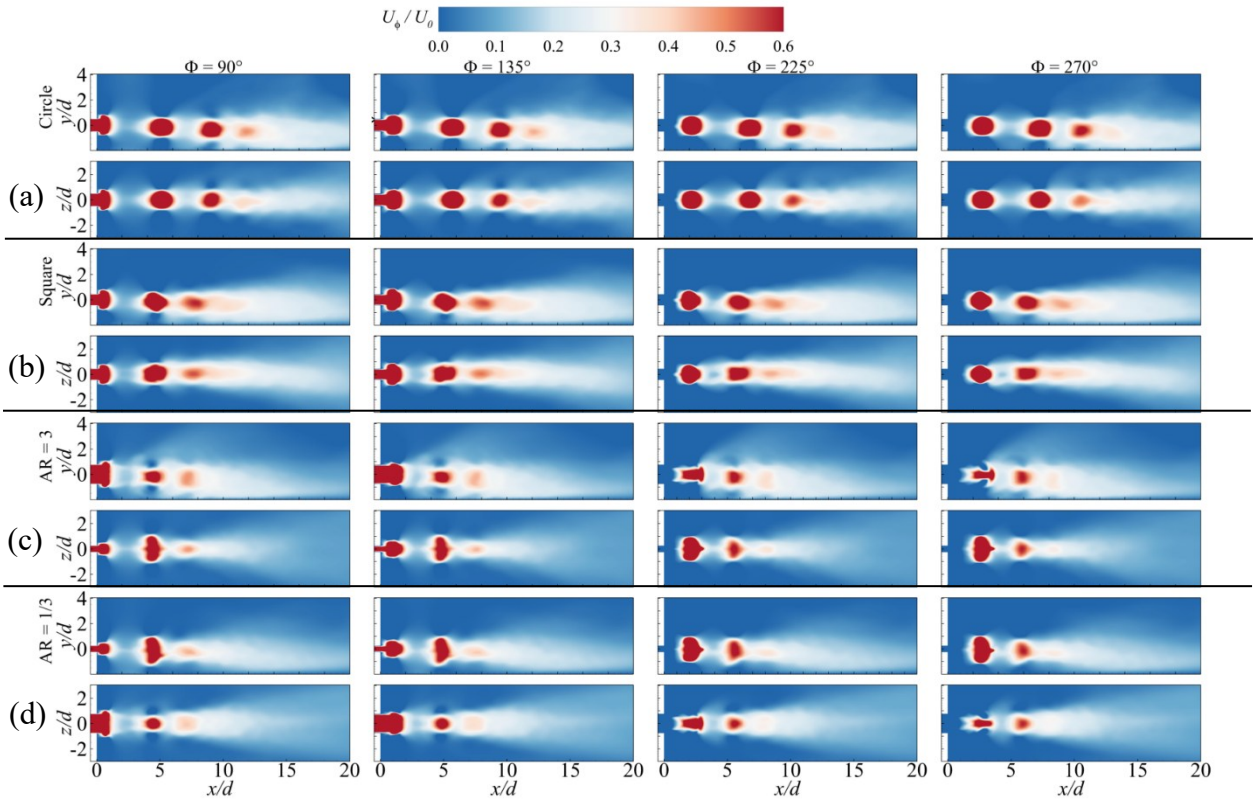

Figure 4.5: Contours of phase-averaged streamwise velocity ($U_\phi/U_0 = 0.46$) for cases: Circle, Square, $AR = 3$ and $AR = 1/3$, in the $x-y$ symmetry plane and the $x-z$ plane at $y/d = 0$.

The plots also show that the self-induced velocity of the expelled vortex decreases as the jet evolves downstream for the non-circular jets compared to the circular jet, with the effect being

more pronounced in the rectangular jets. In particular, at $\phi = 225^{\circ}$, the centroid of the first bulb of velocity is at similar streamwise location for each case. However, the center-to-center distance between the first and second velocity bulbs decreases from $4.5d$ for the circular jet to $4d$ for the square ($4d$), and $3.75d$ for the rectangular cases.

Time-averaged statistics

4.1.1 Contours of mean velocities and turbulence statistics

Contours of the normalized streamwise mean velocity (U/U_0) in the $x-y$ ($z/d = 0$) and $x-z$ ($y/d = 0$) planes for each test case are presented in Figure 4.6. The isopleth of $U/U_0 = 0.01$ is superimposed on the contours to define the jet boundaries.

For each test case, the maximum velocity (U_p) is located downstream of the jet exit due to vena contracta effects. The normalized maximum velocity (U_p/U_0) in the $x-y$ plane is similar for the circular and square jets ($U_p/U_0 = 0.57$), but reduces to 0.53 for $AR = 1/3$ and $AR = 3$.The potential core region is uniform for the circular and square jets; however, for $AR = 3$, the $x-y$ plane shows contraction to a local minimum followed by expansion, while the $x-z$ plane exhibits the opposite pattern. For $AR = 1/3$, the potential core region exhibits the opposite pattern to that of $AR = 3$ in both planes. These expansions and contractions are artefacts of axis switching in the rectangular jets.

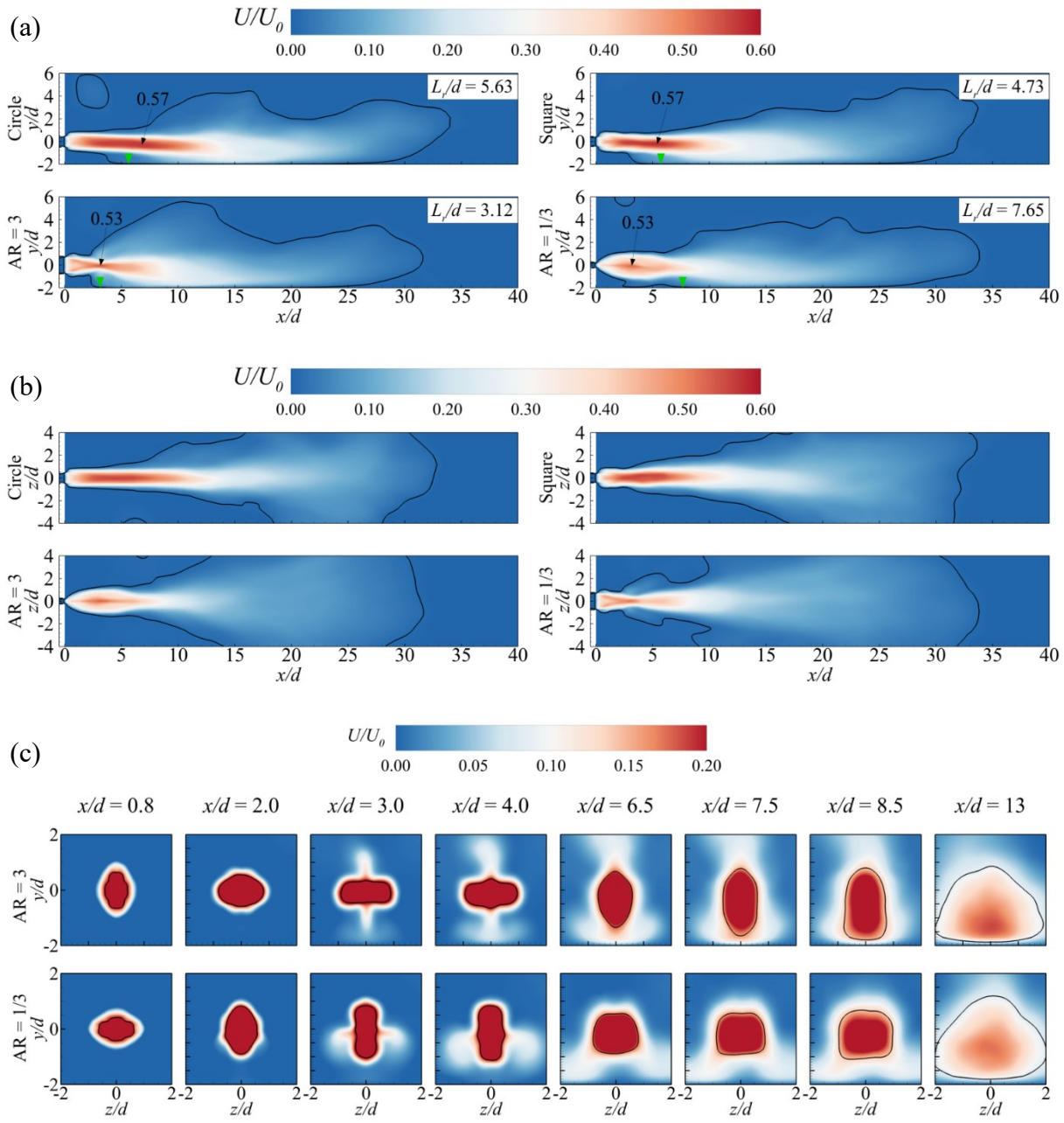

Figure 4.6: Contours of normalized streamwise mean velocity (U/U_0) for all cases in the (a) $x-y$ symmetry plane and the (b) $x-z$ plane at $y/d = 0$. The green arrow indicates the attachment point (x_{rp}). An isopleth of $U/U_0 = 0.01$ is highlighted in black. (c) Contours of U/U_0 in the cross-plane $(y-z)$ at selected streamwise positions. The isopleth of $U_m/U_0 = 0.5$ is superimposed to show the azimuthal jet half-width.

The potential core length (L_p) is defined as the streamwise distance from the nozzle exit to the downstream location where the velocity is $0.9U_p$ ([55]). The potential core length is $L_p/d = 7.75$ for the circular jet but decreases significantly by 19% ($L_p/d = 6.25$) for the square jet. The rectangular jets, on the other hand, exhibit much larger reduction of 45% ($L_p/d = 3.50$) compared to the circular jet. This reduction is attributed to self-induced deformation in the non-circular jets and axis switching in the rectangular jets.

Figure 4.6(a) also depicts that each jet bends and attaches the wall. The attachment length (L_r/d) is determined as the streamwise distance from the nozzle exit to the attachment point (x_{rp}) identified as the location where the $U/U_0 = 0.01$ isopleth permanently intersects the wall, as indicated by the green arrows in the $x - y$ plane. The attachment length is $L_r/d = 5.63$ for the circular jet but reduces to $L_r/d = 4.73$ for the square jet. As a result of axis switching, the attachment length decreases substantially by 45% for AR = 3 ($L_r/d = 3.12$), but increases by 36% for $AR = 1/3$ ($L_r/d = 7.65$) compared to the circular jet.

Contours of the streamwise mean velocity in cross-planes ($y - z$) at selected streamwise locations near the nozzle exit ($x/d = 0.8$), at the location of U_p, and further downstream ($x/d = 13$) are used to visualize the axis-switching behaviour of $AR = 3$ and $AR = 1/3$, as shown in Figure 4.6(c) The plots illustrate the transition of the jet from its initial orientation at the exit to the reoriented state following axis switching for each test case.

Figure 4.7 shows the contours of the normalized spanwise ($\omega_z d/U_0$) and wall-normal ($\omega_y d/U_0$) mean vorticities in the vertical and horizontal planes, respectively. The out-of-plane vorticity reveals the shear layers of the jet in each plane and the signs are consistent with the orientation of

the mean shear. The vorticity decreases as the jets evolves downstream due to entrainment and momentum transfer to the surrounding fluid. Near the wall, the CW vorticity is entrained into the boundary layer beyond the attachment point x_{rp}. The entrained vorticity builds up on the wall as the wall synthetic jet develops before decaying further downstream. For $AR = 3$ and $AR = 1/3$, the effects of axis switching are evident in the contraction and expansion of the intense vorticity regions between the two planes.

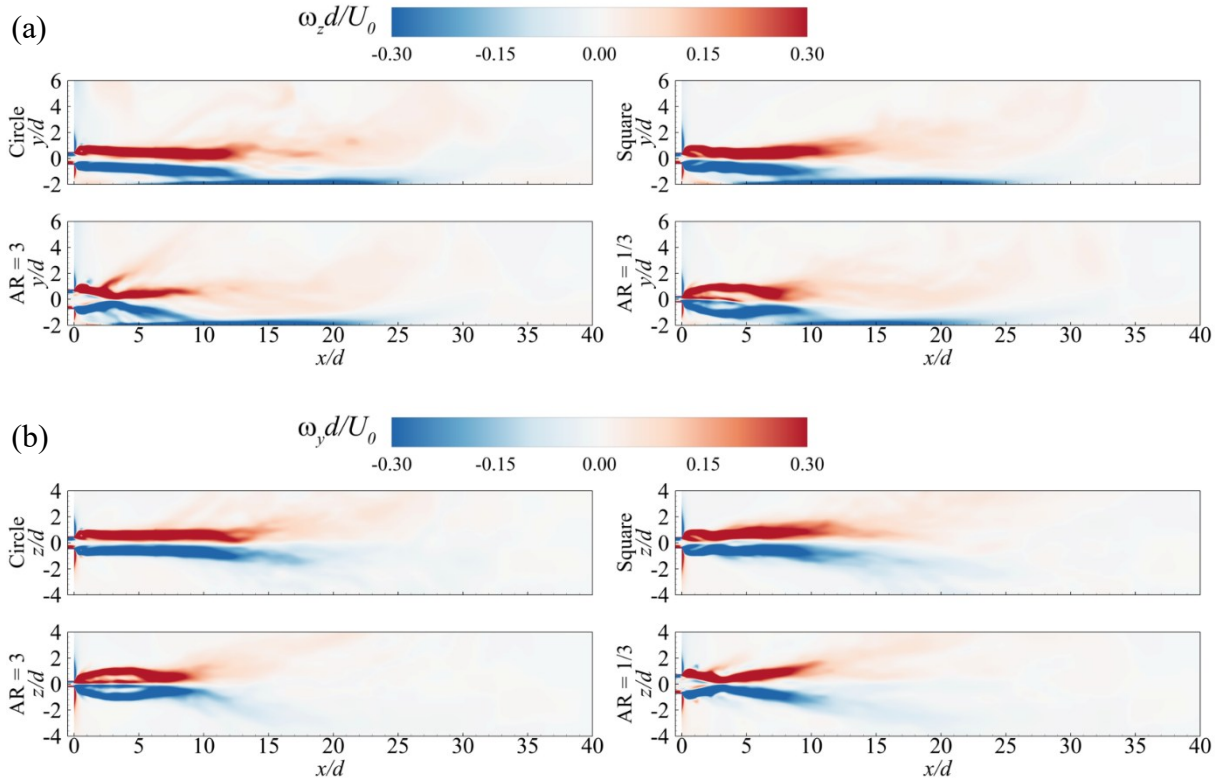

Figure 4.7: Contours of (a) normalized spanwise vorticity ($\omega_z d/U_0$) and (b) wall normal ($\omega_y d/U_0$) vorticity for all test cases in the (a) $x-y$ symmetry plane and the (b) $x-z$ plane at $y/d = 0$.

Contours of the normalized turbulent kinetic energy (TKE/U_0^2) in both the $x-y$ and $x-z$ planes are presented in Figure 4.8. The turbulent kinetic energy is determined as $0.5(\overline{uu} + \overline{vv} + \overline{ww})$,

where $\overline{uu}$, $\overline{vv}$ and $\overline{ww}$ are the streamwise, wall-normal and spanwise Reynolds normal stresses. The TKE is more intense in the near field and decays rapidly downstream, in agreement with the experimental results of Lui et al. [56] This behavior is attributed to the alternating ingestion and expulsion of fluid in the near field, which generate strong periodic fluctuations and promote shear-layer roll-up into vortex rings, thereby inducing large mean shear near the jet exit.

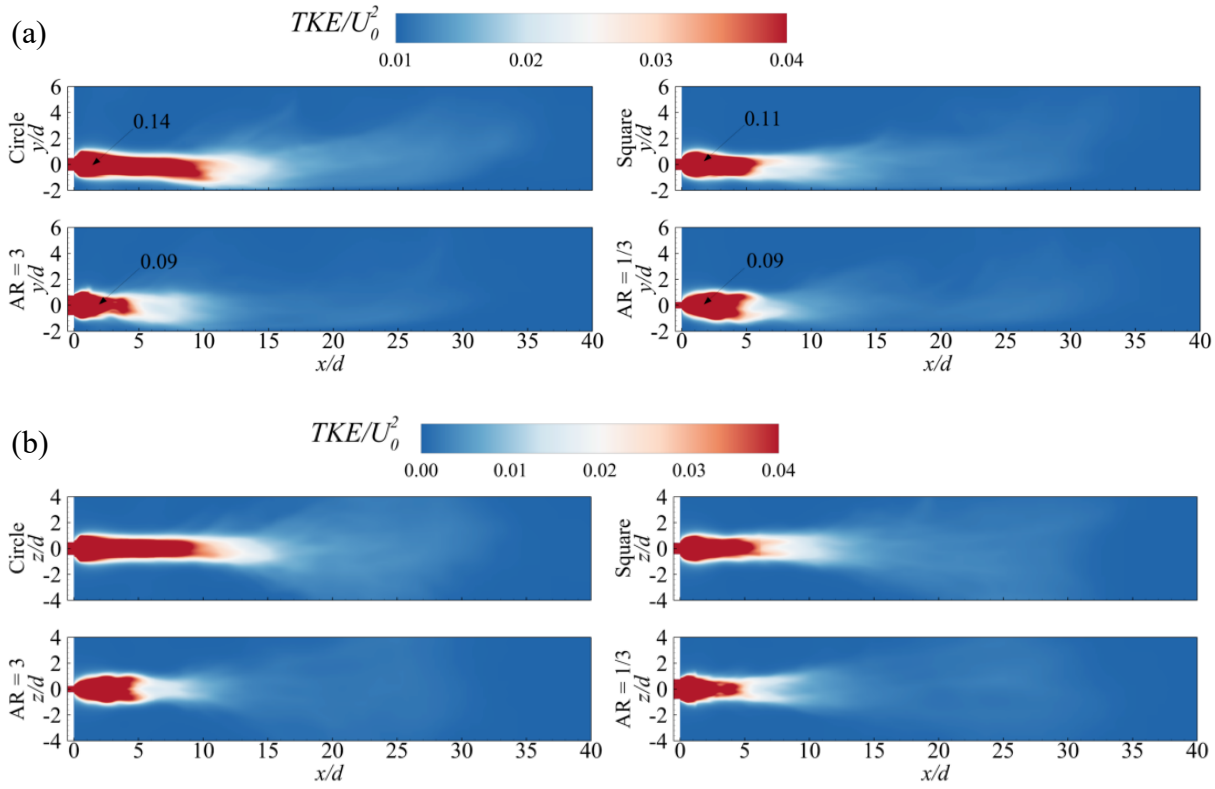

Figure 4.8: Contours of normalized turbulent kinetic energy (TKE/U_0^2) for circle, square, $AR = 3$ and $AR = 1/3$, in the (a) $x - y$ symmetry plane and the (b) $x - z$ plane at $y/d = 0$.

The TKE is more intense and extends farther downstream for the circular jet compared to the other test cases, consistent with the persistence of the vortex rings observed for the circular jet (Figures 4.2 and 4.4). Axis switching leads to a wider spatial spread of TKE in the plane aligned with the

reoriented vortices; however, the TKE decays more rapidly in the rectangular jets than in both the square and circular jets.

Figure 4.9 presents contours of normalized Reynolds shear stress ($-\overline{uv}/U_0^2$) in the $x-y$ and $x-z$ planes for each test case. Unlike steady jets, the Reynolds shear stress in synthetic jets is not continuously distributed within the shear layer due to the periodic generation and evolution of vortex rings. For all cases, the lower shear layer, characterized by negative Reynolds shear stress, interacts with the wall; however, this region is more pronounced and persists longer in the circular jet than in the other jets.

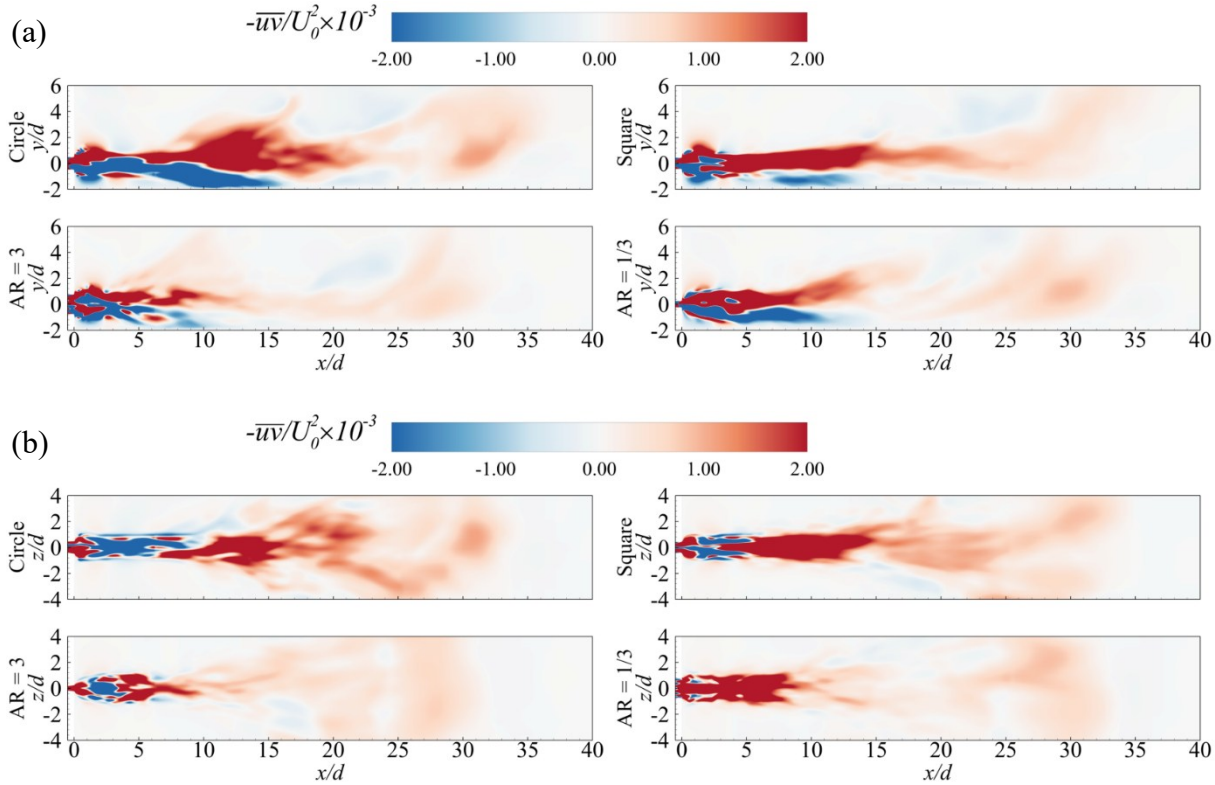

Figure 4.9: Contours of normalized Reynolds shear stress ($-\overline{uv}/U_0^2$) for circle, square, $AR = 3$ and $AR = 1/3$, in the (a) $x-y$ symmetry plane and the (b) $x-z$ plane at $y/d = 0$.

Following wall interaction, the negative Reynolds shear stress rapidly decays while the positive Reynolds shear stress is enhanced. This decay occurs more rapidly for the square and $AR = 3$ cases, whereas the $AR = 1/3$ case remains more persistent than these configurations due to the orientation of the vortex after axis switching

Offset synthetic jet decay and spread

The decay of the offset jets is examined using profiles of the local maximum streamwise mean velocity (U_m) presented in Figure 4.10. The profiles are normalized using d and U_0 as the velocity and length scales, respectively. For each test case, the maximum velocity rapidly increases from near-zero values at the nozzle exit, due to the zero-net-mass-flux nature of synthetic jets, to a global maximum associated with the location of vortex ring formation. Further downstream, the maximum velocity decays with increasing streamwise distance, exhibiting behavior similar to that observed in free synthetic and steady jets [57]. The profiles demonstrate that the local maximum velocities are higher for the circular synthetic jet than for the non-circular jets, while the rectangular jets exhibit similar but lower velocities compared to the square jet.

Following Glezer & Amitay [5] and Agelin-Chaab & Tachie [30], the decay rate of the offset synthetic jets can be described by a power law given as $(U_m/U_0) \propto (x/d)^{-n}$, where n is the decay rate. Table 3.1 summarizes the decay rate for each offset synthetic jet. The decay rate for the circular offset synthetic jet is $n = 1.34$, which is approximately 15% larger than $n = 1.17$ reported for an offset steady jet at a comparable offset ratio of $2d$ [33]. Although the previous steady jet study [33] was conducted at a higher Reynolds number, the larger decay rate suggests enhanced mixing for the synthetic jet compared to the steady jet. For the non-circular synthetic jets, the decay rate is reduced by approximately 8% and 33% for the square ($n = 1.24$) and

rectangular ($n \approx 0.90$) jets, respectively, compared to the circular jet. These reductions may be attributed to earlier interaction with the wall, promoting the growth of the wall synthetic jet, which leads to a reduced decay rate.

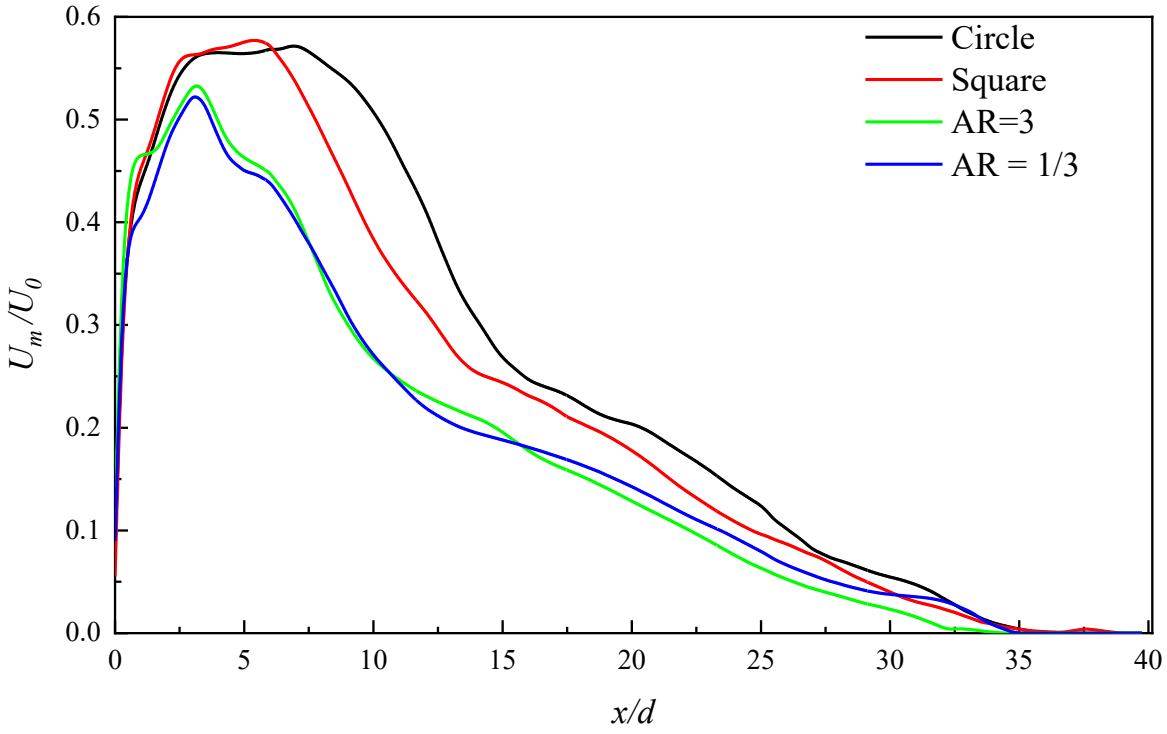

Figure 4.10: Streamwise evolution of the normalized maximum mean streamwise velocity (U_m/U_0) in the $x-y$ symmetry plane.

Table 4.1 Decay rate for the offset synthetic jets

Test Case	Decay Rate ($\boldsymbol{n}$)
Circle	1.39
Square	1.24
$AR = 3$	0.91
$AR = 1/3$	0.89

The spread of the offset synthetic jets are characterized using the jet half-width, $y_{0.5}/d$, in the $x-y$ (vertical) plane, as shown in Figure 4.11. The jet width is defined as the wall-normal distance from the location of U_m to the position where the velocity is $0.5U_m$ in the outer shear layer of the jet. Unlike steady jets, the half-width of the synthetic jet increases nonlinearly due to the periodic evolution of the jet. In the near field, $AR = 3$ demonstrates a local reduction, whereas $AR = 1/3$ shows a local increase in the region, $x/d \in [1,6]$, consistent with the axis-switching region of these jets. Further downstream, the profiles do not exhibit a consistent dependence on nozzle geometry.

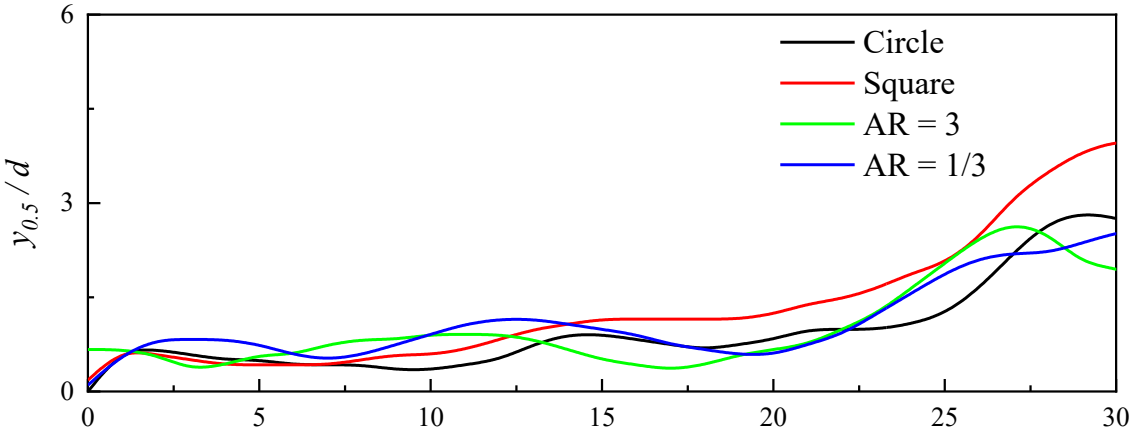

Figure 4.11: Streamwise evolution of the jet half-width ($y_{0.5}/d$) in the $x-y$ symmetry plane for each test cases.

Profiles of offset synthetic jet evolution

The effects of nozzle geometry on the evolution of the offset synthetic jets are examined using profiles of the streamwise mean velocity at selected streamwise locations in the $x-y$ ($z=0$) and $x-z$ ($y=0$) planes as shown in Figure 4.12. To facilitate comparison, the first profile location,

denoted as $\tilde{x}/d = 0$ was selected at $x/d = 0.4$ for the square and circular cases, and at $x/d = 0.8$ for cases $AR = 3$ and $AR = 1/3$. Subsequent profile locations were offset from this initial location. In Figures 4.12(a) and (b), the profiles are normalized by the maximum jet exit velocity, U_0, to examine the jet evolution for each test case. However, in Figure 4.12(c), the local maximum velocity, U_m, is used to characterize the development of the wall synthetic jet and to assess similarity across the various test cases.

In the $x - y$ plane (Figure 4.12(a) and (c)), the velocity profiles for all test cases show the transition from an offset jet profile in the near field to a wall synthetic jet profile in the far field, consistent with results reported for offset steady jets [30]. In the $x - z$ plane (Figure 4.12(b), the profiles are symmetric about $y/d = 0$. In the near field ($\tilde{x}/d \leq 7$), the circular and square jets exhibit a top-hat profile at $\tilde{x}/d = 0$, which gradually transitions to a Gaussian-like distribution about the local maximum velocity. The rectangular jets exhibit a top-hat profile along the initial major axis and a contracted profile along the minor axis at $\tilde{x}/d = 0$ in both planes. Downstream, the profiles contract in the initial major-axis plane and expand in the initial minor-axis plane, indicating axis switching. As a result, peak velocities for the rectangular jets decrease earlier, and wall interaction occurs sooner, particularly for $AR = 3$. Further downstream ($\tilde{x}/d \geq 22$), the rectangular-jet profiles recover and approach those of the square and circular jets (Figures 4.12 (a) and (b)).

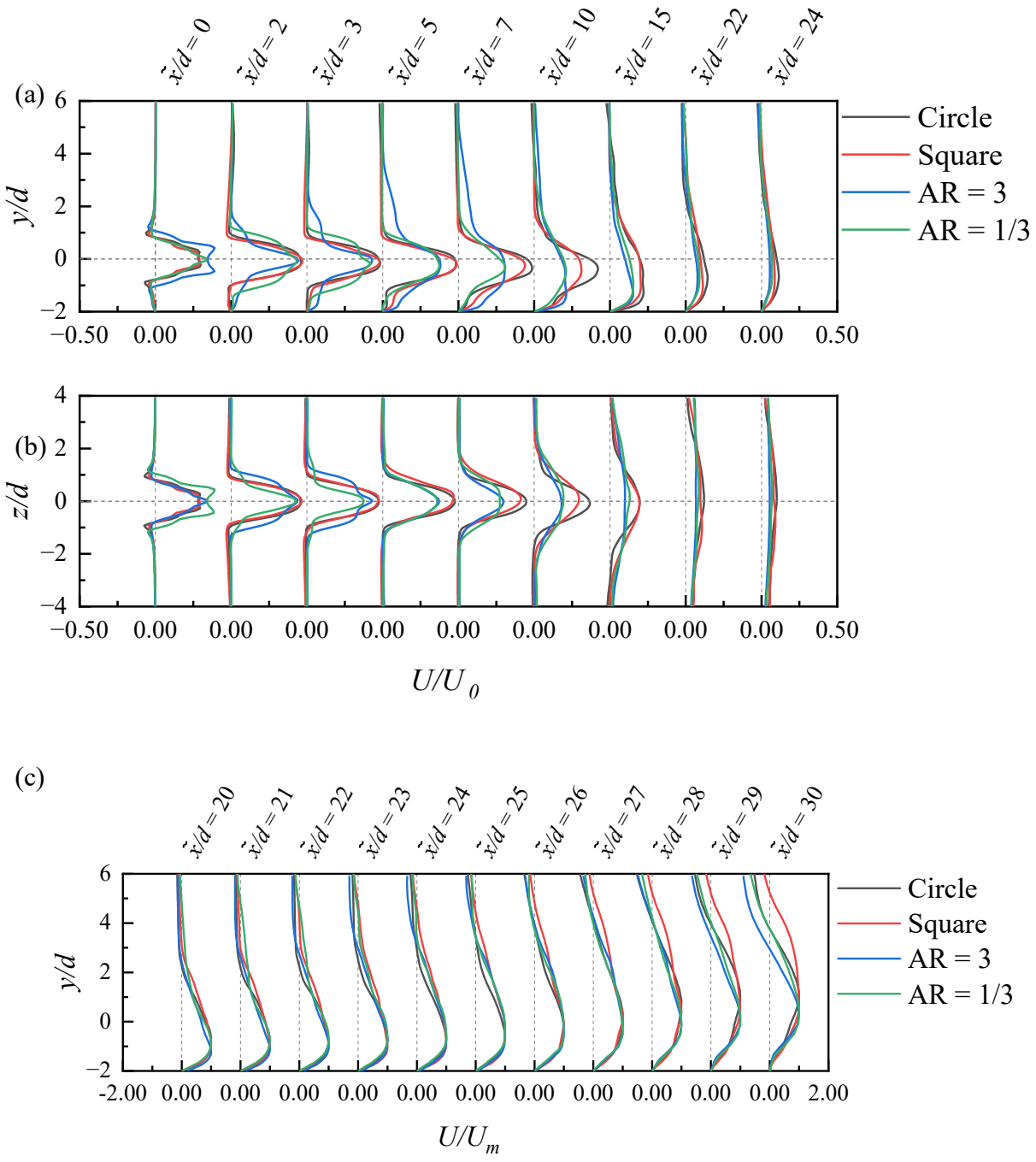

Figure 4.12: Profiles of the normalized streamwise mean velocity (U/U_0) for each test cases in the (a) $x-y$ symmetry plane and the (b) $x-z$ plane at $y/d = 0$. (c) Profiles of streamwise mean velocity normalized with the maximum velocity (U_m/U_0) in streamwise range, $20 \leq \tilde{x}/d \leq 30$.

In Figure 4.12(c), the profiles demonstrate remarkable similarity among the different test cases within $\tilde{x}/d \in [20,27]$, before diverging in the outer layer of the wall synthetic jet further downstream. This suggests self-similarity and a stronger influence of the wall in the wall-jet region. The loci of the local maximum velocities in the profiles also indicate a gradual increase in the boundary-layer thickness of the wall synthetic jet further downstream.

Profiles of the out-of-plane mean vorticity in the $x - y$ and $x - z$ planes are presented in Figure 4.13. In the near field, the vorticity profiles exhibit two dominant, oppositely signed peaks located at the outer shear layers of the offset synthetic jet, accompanied by weaker inner peaks closer to the jet core. As the jet evolves downstream, enhanced turbulent mixing suppresses the inner peaks. Beyond the attachment point, interaction with the wall leads to vorticity growth near the wall. Farther downstream, the near-wall vorticity region merges with the inner shear layer of the jet (negative vorticity) as the flow transitions into a wall synthetic jet. During this transition, overall peak vorticity decreases as a result of turbulent diffusion and momentum redistribution. In the offset and transitional regions, the circular and square jets initially exhibit higher peak vorticity compared to the rectangular jets. For $\tilde{x}/d \geq 15$, however, the vorticity profiles for all test cases collapse reasonably well, indicating a reduced dependence on the initial jet geometry in the developed wall-jet region.

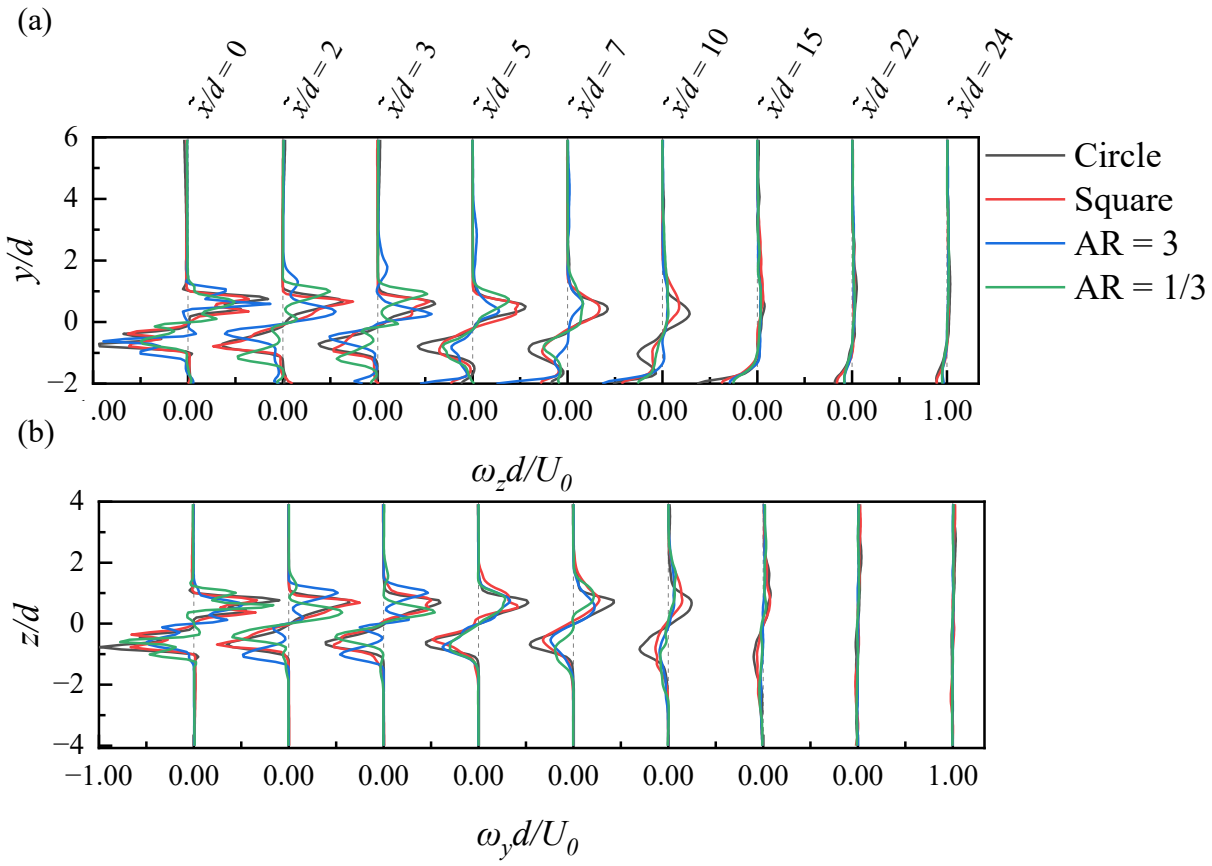

Figure 4.13: Profiles of (a) spanwise mean vorticity ($\omega_z d/U_0$) in the $x-y$ symmetry plane and (b) wall-normal mean vorticity ($\omega_y d/U_0$) in $x-z$ plane at $y/d = 0$ for each test case.

Chapter 5. Conclusions and recommendations

5.1 Summary and conclusions

In this study, the effect of nozzle geometry on the turbulent mixing characteristics of three-dimensional (3D) offset synthetic jets interacting with a wall was investigated using improved delayed detached eddy simulations (IDDES). Four nozzle geometries with identical cross-sectional areas were examined: a circular orifice, a square orifice, and two rectangular orifices oriented such that the major axis was either parallel or perpendicular to the wall. These rectangular configurations correspond to aspect ratios of $AR = w/l = 3$ and $AR = 1/3$, respectively, where w is the width and l is the height of the nozzle. For each test case, the actuation frequency and amplitude were kept constant at f = 300 Hz and a = 32 μm, respectively. The Reynolds number, based on the maximum jet exit velocity U_0, and nozzle diameter d, was $Re_0 = 560$. The offset distance from the center of each nozzle to the bottom wall was kept fixed at $2d$.

In all test cases, the synthetic jet deflected toward the wall and subsequently attached to the surface due to the Coandă effect. The attachment length for the circular nozzle was $L_r/d = 5.63$, but decreased by 16%, 36% and 45% for the square, $AR = 1/3$ and $AR = 3$, respectively. Beyond the attachment point, the jet redeveloped into a wall synthetic jet that exhibited similar behavior across the different test cases further downstream. The mean jet decay rate was $n = 1.34$ for the circular jet and was reduced by 8% and 33% for the square and rectangular jets. Furthermore, the mean velocities, vorticities, and turbulence statistics persisted farther downstream for the circular jet, followed by the square and then the rectangular jets. These results demonstrated enhanced turbulent mixing for the non-circular jets, particularly for the rectangular jets.

Instantaneous and phase-averaged statistics were also analyzed to provide insight into the observed mean flow and turbulent characteristics of the jets. The results showed that the 3D vortex rings generated by the circular jet were more coherent and persisted farther downstream before attaching to the wall. Following attachment, the vortex rings deformed and broke down into smaller structures that stretched in the spanwise direction along the wall before eventually dissipating. Although the square jet exhibited a similar vortex evolution to the circular jet, the vortex rings were less persistent due to self-induced deformation originating from the square nozzle edges. In the case of the rectangular nozzles, the vortex rings underwent axis switching, accompanied by the formation of secondary spanwise vortices both upstream and downstream of the reoriented rings. The enhanced mixing observed in the rectangular jets was attributed primarily to this axis-switching phenomenon.

Furthermore, due to the different orientations of the rectangular nozzles relative to the bottom wall, the interaction between the vortex rings and the wall was stronger for the $AR = 1/3$, leading to more pronounced vortex deformation. In contrast, axis switching in the $AR = 3$, promoted spanwise spreading, redistribution of vorticity, and the development of larger peripheral near-wall structures.

The present study provided valuable physical insight into the effects of nozzle geometry on the evolution of offset synthetic jets interacting with a wall, representing the first such investigation reported in the literature. The findings have the potential to guide the development of effective flow-control strategies for enhancing mixing and heat transfer in fluid-thermal applications, including turbine blade film cooling, electronic cooling systems, and turbulence-control approaches for delaying flow separation on aircraft and ground vehicles.

5.2 Recommended future work

Based on the scope and main findings of this study, the following are recommended for future work:

- Conduct more extensive analyses using advanced statistical tools, such as Proper Orthogonal Decomposition (POD) and Spectral-POD, to extract coherent structures and examine their roles in momentum transfer, mixing, and vortex evolution in offset synthetic jets.
- Investigate the effects of Reynolds number and offset height ratios on rectangular offset synthetic jets exhibiting axis switching to gain deeper insights into the interaction of the vortical structures with the wall.
- Integrate machine learning techniques for predicting and reconstructing low-order representations of offset synthetic jets, enabling more efficient modeling and control of their flow behavior.
- Use machine learning to optimize the actuation parameters of offset jets to further improve their performance in fluid-thermal engineering applications.
- Explore closed-loop control of offset jets over isothermal walls to explicitly examine their impact on heat transfer enhancement.

Bibliography

[1] M. Jabbal and S. Zhong, "The near wall effect of synthetic jets in a boundary layer," *International Journal of Heat and Fluid Flow*, vol. 29, no. 1, pp. 119–130, 2008, doi: https://doi.org/10.1017/S0001924000001305.

[2] M. A. Feero, S. D. Goodfellow, P. Lavoie, and P. E. Sullivan, "Flow reattachment using synthetic jet actuation on a low reynolds number airfoil," *AIAA Journal*, vol. 53, no. 7, pp. 1–26, 2014, doi: https://doi.org/10.1016/j.sna.2014.12.004.

[3] M. Arik and Y. V. Utturkar, "A computational and experimental investigation of synthetic jets for cooling of electronics," *Journal of Electronic Packaging*, vol. 137, no. 2, p. 021005, 2015, doi: https://doi.org/10.1115/1.4029067.

[4] C. Xu, Y. Long, and J. Wang, "Entrainment mechanism of turbulent synthetic jet flow," *Journal of Fluid Mechanics*, vol. 958, p. A31, 2023, doi: https://doi.org/10.1017/jfm.2023.102.

[5] A. Glezer and M. Amitay, "Synthetic Jets," *Annual Review of Fluid Mechchanics*, vol. 34, pp. 503–529, 2001, doi: https://doi.org/10.1146/annurev.fluid.34.090501.094913.

[6] N. Chen and H. Yu, "Mechanism of axis switching in low aspect-ratio rectangular jets," *Computers and Mathematics with Applications*, vol. 67, no. 2, pp. 437–444, 2014, doi: https://doi.org/10.1016/j.camwa.2013.03.018.

[7] R. Kotapati, R. Mittal, and N. L. Cattafesta, "Numerical study of a transitional synthetic jet in quiescent external flow," *Journal of Fluid Mechanics*, vol. 581, pp. 287–321, 2007, doi: doi:10.1017/S0022112007005642.

[8] M. Jain, B. Puranik, and A. Agrawal, "A numerical investigation of effects of cavity and orifice parameters on the characteristics of a synthetic jet flow," *Sensors and Actuators, A: Physical*, vol. 165, pp. 351–366, 2011, doi: https://doi.org/10.1016/j.sna.2010.11.001.

[9] H. Zong and M. Kotsonis, "Characterisation of plasma synthetic jet actuators in quiescent flow," *Journal of Physics D: Applied Physics*, vol. 49, p. 335202, 2016, doi: 10.1088/0022-3727/49/33/335202.

[10] S. Carpy and R. Manceau, “Turbulence modelling of statistically periodic flows: Synthetic jet into quiescent air,” *International Journal of Heat and Fluid Flow*, vol. 27, no. 5, pp. 756-767, 2006, doi: https://doi.org/10.1016/j.ijheatfluidflow.2006.04.002.

[11] T. Van Buren, E. Whalen, and M. Amitay, “Vortex formation of a finite-span synthetic jet: Effect of rectangular orifice geometry,” *Journal of Fluid Mechanics*, vol. 745, pp. 180–207, 2014, doi: https://doi.org/10.1017/jfm.2014.77.

[12] L. Wang, L. H. Feng, J. J. Wang, and T. Li, “Evolution of low-aspect-ratio rectangular synthetic jets in a quiescent environment,” *Experiments in Fluids*, vol. 59, no. 91, pp. 1–16, 2018, doi: https://doi.org/10.1007/s00348-018-2544-x.

[13] H. H. Ho, E. E. Essel, and P. E. Sullivan, “The interactions of a circular synthetic jet with a turbulent crossflow,” *Physics of Fluids*, vol. 34, no. 7, p. 075108, 2022, doi: https://doi.org/10.1063/5.0099533.

[14] Y. Xu, C. Moon, J. J. Wang, O. G. Penyazkov, and K. C. Kim, “An experimental study on the flow and heat transfer of an impinging synthetic jet,” *International Journal of Heat and Mass Transfer*, vol. 144, p. 118626, 2019, doi: https://doi.org/10.1016/j.ijheatmasstransfer.2019.118626.

[15] J. Chang *et al.*, “Investigation of Vortex Rings for Free Jet and Synthetic Jet at Various Reynolds Numbers and Strouhal Numbers,” *Mathematical Problems in Engineering*, vol. 2020, pp. 1–15, 2020, doi: https://doi.org/10.1155/2020/1503628.

[16] J. F. Li, X. B. Zhang, and T. H. New, “Formation and flow characteristics of low-Reynolds number synthetic jets,” *Physics of Fluids*, vol. 37, no. 3, p. 033631, 2025, doi: https://doi.org/10.1063/5.0259436.

[17] C. G. Ball, H. Fellouah, and A. Pollard, “The flow field in turbulent round free jets,” *Progress in Aerospace Sciences*, vol. 50, pp. 1–26, 2012, doi: https://doi.org/10.1016/j.paerosci.2011.10.002.

[18] C. D. Donaldson and R. S. Snedeker, *Survey of Literature on Flow Characteristics of a Single Turbulent Jet Impinging on a Flat Plate*. Washington, DC: National Aeronautics and Space Administration, 1971.

[19] B. L. Smith and G. W. Swift, “A comparison between synthetic jets and continuous jets,” *Experiments in Fluids*, vol. 34, no. 4, pp. 467–472, 2003, doi: https://doi.org/10.1007/s00348-002-0577-6.

[20] J. M. Shuster and D. R. Smith, “Experimental study of the formation and scaling of a round synthetic jet,” *Physics of Fluids*, vol. 19, no. 4, pp. 1–21, 2007, doi: https://doi.org/10.1063/1.2711481.

[21] J. Zhou, H. Tang, and S. Zhong, “Vortex roll-up criterion for synthetic jets,” *AIAA Journal*, vol. 47, no. 5, pp. 1252–1262, 2009, doi: https://doi.org/10.2514/1.40602.

[22] A. Hashiehbaf and G. P. Romano, “Particle image velocimetry investigation on mixing enhancement of non-circular sharp edge nozzles,” *International Journal of Heat and Fluid Flow*, vol. 44, pp. 208–221, 2013, doi: https://doi.org/10.1016/j.ijheatfluidflow.2013.05.017.

[23] L. Mangate, H. Yadav, A. Agrawal, and M. Chaudhari, “Experimental investigation on thermal and flow characteristics of synthetic jet with multiple-orifice of different shapes,” *International Journal of Thermal Sciences*, vol. 140, pp. 344–357, 2019, doi: https://doi.org/10.1016/j.ijthermalsci.2019.02.036.

[24] E. Smyk, J. Wilk, and M. Markowicz, “Synthetic jet actuators with the same cross-sectional area orifices-flow and acoustic aspects,” *Applied Sciences (Switzerland*, vol. 10, no. 11, pp. 1–14, 2019, doi: https://doi.org/10.3390/app11104600.

[25] A. Qayoum and A. Malik, “Influence of the Excitation Frequency and Orifice Geometry on the Fluid Flow and Heat Transfer Characteristics of Synthetic Jet Actuators,” *Fluid Dynamics*, vol. 54, no. 4, pp. 575–589, 2019, doi: https://doi.org/10.1134/S0015462819040086.

[26] L. Wang, L. H. Feng, J. J. Wang, and T. Li, “Parameter influence on the evolution of low-aspect-ratio rectangular synthetic jets,” *Journal of Visualization*, vol. 21, pp. 105–115, 2018, doi: https://doi.org/10.1007/s12650-017-0440-8.

[27] J. C. Straccia and J. A. Farnsworth, “Axis switching in low to moderate aspect ratio rectangular orifice synthetic jets,” *Physical Review Fluids*, vol. 6, no. 5, p. 054702, 2021, doi: https://doi.org/10.1103/PhysRevFluids.6.054702.

[28] M. Jabbal, J. Wu, and S. Zhong, “The performance of round synthetic jets in quiescent flow,” *The Aeronautical Journal*, vol. 110, no. 1108, pp. 385–393, 2006, doi: https://doi.org/10.1016/j.ijheatfluidflow.2007.07.011.

[29] S. Iio, T. Kawamura, M. Matsubara, T. Yoshida, and T. Ikeda, “Vortex Behavior of Pulsating Jets from a Rectangular Nozzle,” *JSME International Journal*, vol. 49, no. 4, pp. 988–994, 2006, doi: https://doi.org/10.1299/jsmeb.49.988.

[30] M. Agelin-Chaab and M. F. Tachie, “Characteristics and structure of turbulent 3D offset jets,” *International Journal of Heat and Fluid Flow*, vol. 32, no. 3, pp. 608–620, 2011, doi: https://doi.org/10.1016/j.ijheatfluidflow.2011.03.008.

[31] A. Cyrus, K. N. Hammond, and E. E. Essel, “Effects of Nozzle Geometry on Turbulent Characteristics of 3D Offset Synthetic Jets,” in *THMT-25 Turbulence, Heat and Mass Transfer*, Tokyo, Japan, 2025. doi: 10.1615/THMT-25.

[32] K. N. D. Hammond, M. O. Sandoval, N. Naeem, and E. E. Essel, “On the turbulent flow characteristics of wall-attaching synthetic jets at varying offset height ratios,” *Physics of Fluids*, vol. 37, no. 11, p. 115105, 2025, doi: https://doi.org/10.1063/5.0297258.

[33] A. Nasr and J. C. S. Lai, “A turbulent plane offset jet with small offset ratio,” *Experiments in Fluids*, vol. 24, pp. 47–57, 1998, doi: https://doi.org/10.1007/s003480050149.

[34] A. Assoudi, S. Habli, N. M. Saïd, H. Bournot, and G. L. Palec, “Experimental and numerical study of an offset jet with different velocity and offset ratios,” *Engineering Applications of Computational Fluid Mechanics*, vol. 9, no. 1, pp. 490–512, 2015, doi: https://doi.org/10.1080/19942060.2015.1071525.

[35] B. Nyantekyi-Kwakye, S. P. Clark, M. F. Tachie, M. Jarrod, and M. Getnet, “Flow characteristics within the recirculation region of three-dimensional turbulent offset jet,” *Journal of Hydraulic Research*, vol. 53, no. 2, pp. 230–242, 2014, doi: https://doi.org/10.1080/00221686.2014.950612.

[36] D. C. Wilcox, *Turbulence modeling for CFD*. San Diego: DCW Industries, 2006.

[37] H. K. Versteeg and W. Malalasekera, *An Introduction to Computational Fluid Dynamics: The Finite Volume Method*. London: Pearson Education, 2007. doi: https://doi.org/10.1063/1.1693899.

[38] Siemens, “STAR-CCM +User Guide,” *Siemens*, 2020.

[39] Pope S. B., *Turbulent Flows*. Ithaca: Cambridge University Press, 2000.

[40] I. Yoo and S. Lee, “Reynolds-averaged navier-stokes computations of synthetic jet flows using deforming meshes,” *AIAA Journal*, vol. 50, no. 9, pp. 1943–1955, 2012, doi: https://doi.org/10.2514/1.J051539.

[41] J. Cui and R. K. Agarwal, “Three-dimensional computation of a synthetic jet in quiescent air,” *AIAA*, vol. 44, no. 12, pp. 2857–2865, 2006, doi: https://doi.org/10.2514/1.14213.

[42] V. N. Vatsa and E. Turkel, “Simulation of synthetic jets using unsteady reynolds-averaged Navier-Stokes equations,” *AIAA Journal*, vol. 44, no. 2, pp. 217–224, 2006, doi: https://doi.org/10.2514/1.13535.

[43] F. R. Menter, “Two-equation eddy-viscosity turbulence models for engineering applications,” *AIAA Journal*, vol. 32, no. 8, pp. 1598–1605, 1994, doi: https://doi.org/10.2514/3.12149.

[44] P. R. Spalart, S. Deck, M. L. Shur, K. D. Squires, M. K. Strelets, and A. K. Travin, “A new version of detached-eddy simulation, resistant to ambiguous grid densities,” *Theoretical and Computational Fluid Dynamics*, vol. 20, no. 3, pp. 181–195, 2006, doi: https://doi.org/10.1007/s00162-006-0015-0.

[45] P. R. Spalart, W. H. Jou, S. R. Allmaras, and M. Strelets, “Comments on thefeasibility of LES for wings, and on a hybrid RANS/LES approach,” in *First AFOSR International Conference on DNS/LES*, Louisiana Tech University, 1997.

[46] M. L. Shur, P. R. Spalart, M. K. Strelets, and A. K. Travin, “A hybrid RANS-LES approach with delayed-DES and wall-modelled LES capabilities,” *International Journal of Heat and Fluid Flow*, vol. 29, no. 6, pp. 1638–1649, 2008, doi: https://doi.org/10.1016/j.ijheatfluidflow.2008.07.001.

[47] M. A. Feero, P. Lavoie, and P. E. Sullivan, “Influence of cavity shape on synthetic jet performance,” *Sensors and Actuator," A: Physical*, vol. 223, pp. 1–10, 2015, doi: https://doi.org/10.2514/1.J053605.

[48] N.A.S.A., “Uncertainty and Error in CFD Simulations.” Feb. 10, 2021. [Online]. Available: https://www.grc.nasa.gov/www/wind/valid/tutorial/errors.html.

[49] J. C. R. Hunt, A. A. Wray, and P. Moin, “Eddies, stream, and convergence in turbulent flows,” in *Center for Turbulence Research Proceedings of the Summer Program*, Stanford University, CTR, 1988.

[50] J. Zhou, R. J. Adrian, S. Balachandar, and T. M. Kendall, “Mechanisms for generating coherent packets of hairpin vortices in channel flow,” *Journal of Fluid Mechanics*, vol. 387, pp. 353–396, 1999, doi: doi:10.1017/S002211209900467X.

[51] J. Jeong and F. Hussain, “On the identification of a vortex,” *Journal of Fluid Mechanics*, vol. 285, pp. 69–94, 1995, doi: https://doi.org/10.1017/S0022112095000462.

[52] P. Chakraborty, S. Balachandar, and R. J. Adrian, “On the relationships between local vortex identification schemes,” *Journal of Fluid Mechanics*, vol. 535, pp. 189–214, 2005, doi: doi:10.1017/S0022112005004726.

[53] R. J. Arms and F. H. R, “Localized-Induction Concept on a Curved Vortex and Motion of an Elliptic Vortex Ring,” *Physics of Fluids*, vol. 8, no. 4, pp. 553–339, 1965, doi: https://doi.org/10.1063/1.1761268.

[54] Viets H. and Sforza P. M., “Dynamics of Bilaterally Symmetric Vortex Rings,” *Physics of Fluids*, vol. 15, no. 2, pp. 230-240, 1972, doi: https://doi.org/10.1063/1.1693899.

[55] M. Kim, H. Lee, and W. Hwang, “Experimental study on the flow interaction between two synthetic jets emanating from a dual round orifice,” *Experimental Thermal and Fluid Science*, vol. 126, p. 110400, 2021, doi: https://doi.org/10.1016/j.expthermflusci.2021.110400.

[56] Y. Liu, Z. Ji, H. Wang, Z. Yu, and F. Shan, “On the three-dimensional flow evolution of a submerged synthetic jet with two circular orifices,” *Physics of Fluids*, vol. 36, p. 015110, 2024, doi: https://doi.org/10.1063/5.0183536.

[57] B. L. Smith and A. Glezer, “The formation and evolution of synthetic jets,” *Physics of Fluids*, vol. 10, no. 9, pp. 2281–2297, 1998, doi: https://doi.org/10.1063/1.869828.